Technische Universität München
Department of Aerospace and Geodesy
Fakultät für Luftfahrt, Raumfahrt und Geodäsie
Univ.-Prof. Dr.techn. Mag.rere.nat. Roland Pail

Investigations of the DInSAR derived grounding line migration in Antarctica induced by ocean tides

Yin Ying Ip

Master's Thesis

Master's Course in Earth Oriented Space Science and Technology

Supervisor(s): 1. Prof. Dr. Michael Eineder
German Aerospace Center (DLR)

2. Dr. Dana Floricioiu
German Aerospace Center (DLR)

Date of submission: June, 2021

Statement of Authorship

This thesis is a presentation of my original research work. Wherever contributions of others are involved, every effort is made to indicate this clearly, with due reference to the literature, and acknowledgement of collaborative research and discussions.

Munich, ...21 Jun 2021.... (date)

Author ....(signature)

ACKNOWLEDGEMENTS

Throughout the writing of this thesis I have received a great deal of support and assistance.

First, I would like to express my gratitude Dr. Dana Floricioiu, who has offered me the opportunity to do this thesis and support me all the way while writing. Her insightful feedback has sharpened my thinking and brought this thesis to a higher level. Special thanks to Prof. Michael Eineder, who has introduced me to SAR technology during ESPACE lesson in the first place, arousing my interest of doing a master thesis on SAR.

I would like to thank Dr. Lukas Krieger, who has provided me many supports and always has an open door for discussions. He has provided me many valuable opinions and assisted me during the development of the algorithms.

Thanks to Dr. Yuting Dong, who has provided me useful papers for finishing this thesis.

Marking the end of my study in the ESPACE program, I would like to thank all of my ESPACE colleagues. They are a bunch of nice people and I learnt a lot from them.

ABSTRACT

A grounding line is the boundary between ice resting on a bedrock and floating ice. The migration of the glacier grounding line is an important indicator of ice sheet stability in a warming climate. A retreat of the grounding line location (GLL) observed over long periods (years to decades) might indicate processes related to ice thinning at the surface or underneath of a glacier. Yet, grounding line in nature is not static in position and it is moving also at short time scale namely back and forth with the ocean tidal cycle. Due to the presence of ice shelves, about 76% of the coastline of Antarctica comprises grounding lines, along which the glacial ice experiences tidal flexure. The objective of this thesis is to summarize and analyze the observations of short-term changes of GLL and ocean tides at specific selected sites in Antarctica, and thus eventually find out how ocean tides contributes to short-term GLL migration.

In this study, time series of grounding lines were manually delineated from Sentinel-1 A/B double difference interferograms acquired in 2020. Ocean tide level in each corresponding period was computed from the CATS2008 tide model with air pressure correction from NCEP reanalysis data. To support the analysis, bedrock topography and slope information was extracted from BEDMAP2 bed elevation map at the delineated GLL. In order to perform a quantitative analysis, novel algorithms were developed for generating a reference GLL and calculating GLL migration. The reference GLL generation algorithm generates a concave hull polygon around the GLL datasets, and then perpendicular lines (normals), intersecting GLL segments, along the medial axis of the polygon. Averaging the intersecting points of each normal, a reference line is created by connecting all averaged points. The migration of GLL was estimated using three methods: point-line method, box method and normals outputted when generating the reference GLL.

The reference GLL generating algorithm is robust and the performance was satisfactory. The estimation of GLL migration with the different methods was in good agreement, which indicates they have similar level of robustness. In the investigated areas the estimated short-term displacement was in the order of kilometers, which is the same as the long-term migration. This result indicates the importance of averaging the GLL, as a robust

representation of the GLL in a certain period, when quantifying the long-term migration and drawing conclusions about grounding line retreat and ice thinning.

Although significant short-term migration is observed, the observations considered in this study are insufficient to explain the relationship between ocean tides and GLL migration. Therefore, for future studies, considering additional information, in particularly assimilating numerical model like the elastic beam model, which contains information on the physical processes related to ice bending, becomes necessary in order to reveal the mechanism of the tidal induced GLL migration underneath the ice.

TABLE OF CONTENTS

LIST OF FIGURES

LIST OF TABLES

TERMINOLOGY AND ABBREVIATION

Abbreviation	Definition
AIS_cci	Antarctic Ice Sheet Climate Change Initiative
ASAID	Antarctic Surface Accumulation and Ice Discharge
CATS2008	Circum-Antarctic Tidal Simulation
DEM	Digital Elevation Model
DInSAR	Differential Interferometry[1]
	Double Different Interferometry
DLR	German Aerospace Center
DTED-3	Digital Terrain Elevation Data Level 3
ESA	European Space Agency
EW	Extra Wide Swath Mode
GLAS	Geoscience Laser Altimeter System
GLL	Grounding Line Location
GPS	Global Positioning System
GZ	Grounding Zone
HRTI	High Resolution Terrain Information
IMBIE	Ice sheet Mass Balance Inter-Comparison Exercise
InSAR	SAR Interferometry
IW	Interferometric Wide Swath Mode

---

[1] Common terminology. Not used in this thesis.

IWAP	Integrated Wide Area Processor
LOS	Line of Sight
MEaSUREs	Making Earth System Data Records for Use in Research Environments
MOA	Mosaic of Antarctica
MODIS	Moderate Resolution Imaging Spectroradiometer
NASA	National Aeronautics and Space Administration
NCEP	National Centers for Environmental Prediction
PRF	Pulse Repetition Frequency
RAMP	RADARSAT-1 Antarctic Mapping Project
RAR	Real Aperture Radar
RMS	Root Mean Square
RSS	Residual Sum of Squares
SAR	Synthetic Aperture Radar
SARIn	Synthetic Aperture Radar Interferometric
SM	Stripmap Mode
TanDEM-X	TerraSAR-X add-on for Digital Elevation Measurement
TOPSAR	Terrain Observation by Progressive Scan
WV	Wave Mode

CHAPTER 1
Introduction

1.1 Motivation

Monitoring glaciers is essential in the climate change era. When years of snow has fallen and is compressed on the ground, the snow is eventually transformed into a large, thicken and compressed glacial ice. Currently, 10% of land area on Earth is covered by glacial ice, including polar regions, such as the Artic, Greenland and Antarctica, and mountain ranges like the Alps and the Himalayas.

Glacial ice can be found in nature in various forms and sizes from isolated glaciers to ice fields, ice caps and ice sheets. At present, on Earth there are only two ice sheets, Greenland and Antarctica, comprising about 99% of Earth's glacial ice (Panchuk, 2019). Associated with an ice sheet, glacial ice has different characteristics. An ice shelf forms when an ice sheet flows over the underlying bedrock and becomes a floating platform on the ocean water. Ice shelves are surrounding 76% of the Antarctic continent (Rignot et al., 2011) and are present at a much more reduced extent in Greenland. An ice stream is a ribbon-like fast-moving section of an ice sheet (Panchuk, 2019) responsible for the majority of the ice that leaves the sheet.

As part of the world water cycle, glaciers are a prominent resource of natural fresh water. According to the estimation of (Gleick, 1993), around 68% of global fresh water is stored in glacial ice. Therefore, melting of glaciers means releasing a large amount of fresh water, which likely end-up entering the ocean and leads to sea level rise, which has devastating effects on coastal habitats. Beside resulting in a rising sea level, the deep-water formation at the Arctic and Antarctica circulation might also be shut down. As the driving force of the global thermohaline circulation, the deep-water formation is solely depending on the buoyancy of water mass. In other word, deep-water forms only if the water mass is dense enough to sink. Therefore, deep-water formation is not favorable under decreasing salinity, due to the increasing amount of fresh water, which makes the water mass less dense. While

the result of glacial melting could be disastrous, a long-term monitoring of glaciers helps scientists to better understand the response of glacial ice to regional and global climate, and to improve the current used climate models (Bryan, 1986).

Monitoring glaciers is a broad and extensive field of work, and some parameters are complicated to observe. Glacial ice is more than just a static mass of ice, which forms when there is snow accumulation and melts when the environment is warm; it is dynamic, flowing from the thickest region to thinner region at the ice margins. In fact, comparing to other geological processes, which are occurring in geological time scale (thousands to millions of years), glacier is changing much quicker, in a time-span of a human life. Information on ice dynamics is needed, therefore monitoring only the size and extent of glacier is insufficient. Features that provide information understanding glacial ice dynamics and revealing events happening underneath the ice are valuable for glaciological studies. One wants to first break down the broad field of 'monitoring glacier' into many pinpointed scientific questions, such as: how can one detect the potential melting under ice shelves?

Addressing the above question, the boundary between grounded ice and ice shelf, also known as the grounding line is often of interest (Fricker et al., 2009). Nowadays, only the Antarctic Ice Sheet is largely surrounded by ice shelves of various sizes and displays about 22600 km of grounding line (Rignot et al., 2011). On the other hand, only few ice shelves are still present in Greenland. Therefore, the grounding line can be considered a significant feature for Antarctica only.

The grounding line location (GLL) reveals the portion of glacial ice floating, which is inherently less stable and in the risk of calving and collapse. When studying ice sheets, knowing GLL is essential for various reasons. One is in defining the boundary where ice discharge and ice flux into the ocean are calculated. In ice sheet numerical modeling it represents the transition from basal friction at the bed to frictionless sliding on water. Most importantly, a retreat of GLL is a consequence of the migration of hydrostatic equilibrium and could indicate the thinning of the grounded ice in a warming climate. Therefore, GLL is also considered as an indicator of climate change.

However, it is important for scientists to take other factors that could potentially affect GLL and its displacement into account before drawing the conclusion that the retreat of GLL is a result of changes due to regional or global climate warming. GLL is moving naturally backwards and forwards with the ocean tidal cycle. Rignot et al. have reported observation of short-term GLL migration of 2-3 km in 2011.The range of this movement is depending on several factors like the amplitude of the ocean tide, air pressure and subglacial topography.

The aim of this thesis is to assess the short-term movements of the GLL due to the ocean tides in Antarctica and to provide a range of parameters characteristic to this displacement. The results presented in this study should provide a support to further investigations related to climate induced GLL migration by facilitating the separation among several causes of its displacement. In other words, in order to filter out the signal of GLL retreat due to climate change, the contribution of ocean tides should be estimated first.

1.2 The Antarctic Ice Sheet
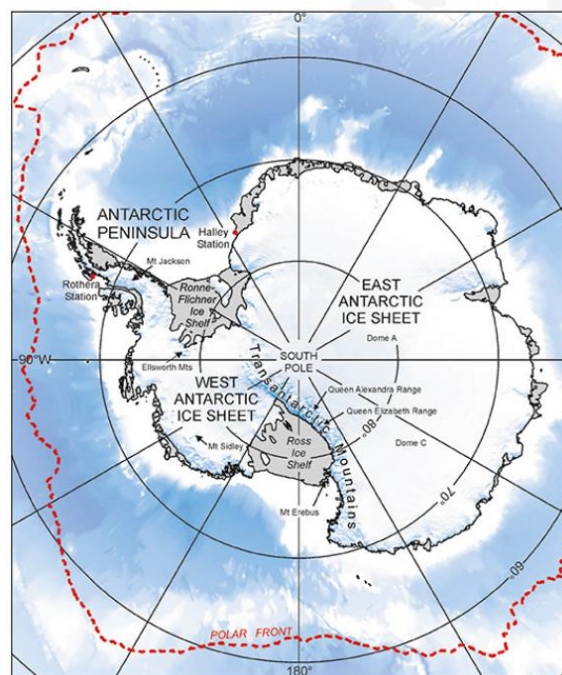
Figure 1-1 Antarctica's main features (British Antarctic Survey, 2005).The ice shelves are shown in grey.

Antarctica, Earth's southernmost continent (Figure 1-1) can be divided into three major areas: West and East Antarctica, and the Antarctic Peninsula. A mountain chain, the Transantarctic Mountains, extends from the Southern end of the Peninsula across the continent and serves as a natural divide between the East and West Antarctic Ice Sheets. Ice flows from the high plateau of East Antarctica through the fjords of the Transantarctic Mountains into the Ross Ice Shelf and thus being exported into the ocean.

Atmospheric warming and changes in ocean conditions during the past decades were reported for the Antarctic Peninsula (Cook & Vaughan, 2010). East Antarctica is considerably larger, yet more stable in terms of mass change than the rest of Antarctica (Figure 1-2). Multiple studies like e.g. those summarized in the Ice sheet Mass Balance Inter-Comparison Exercise (IMBIE) Project (Shepherd et al., 2018) and (Rignot et al., 2014) have shown that West Antarctica is the dominant contributor to the mass loss from the Antarctic ice. One of the reasons of the loss, significant also for the present study, is the shape and elevation of bedrock beneath the ice. Many glaciers in West Antarctica, e.g. Pine Island, Thwaites, Smith, and Kohler glaciers, are grounded on a retrograde bed slope, which the elevation decreases landward. As the freezing point of seawater drops with increase water pressure (Fofonoff & Millard Jr, 1983), glacial ice lying on a retrograde bedrock is inherently unstable.
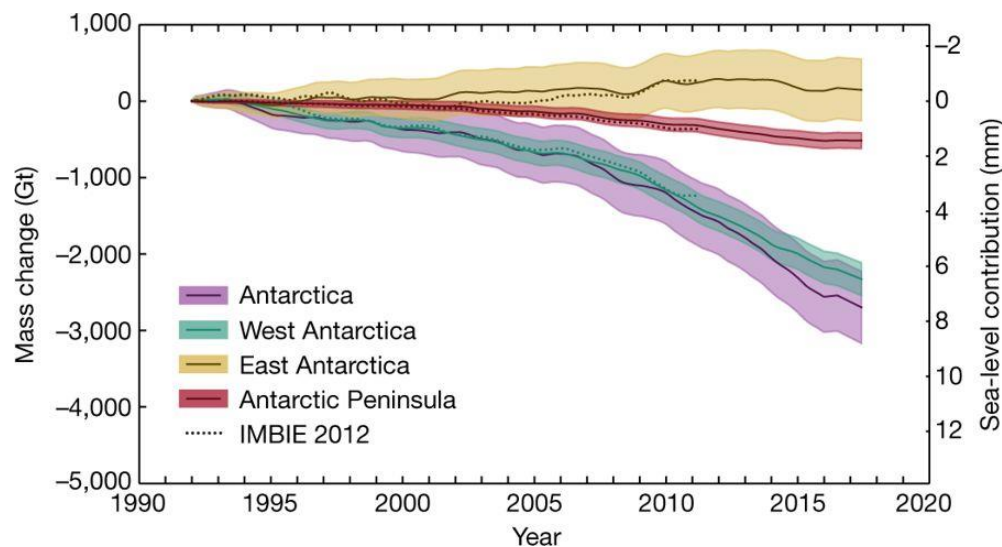
Figure 1-2 Mass changes in Antarctica resulted from the combination of satellite-based techniques in the IMBIE Project Phase 2 (Shepherd et al., 2018).

Detecting the GLL is a difficult task because of the lack of surface features indicating its presence. As shown in Figure 1-3, the transition from grounded to floating ice is not visible at the surface. Various techniques based on satellite data developed to detect indirectly the GLL are presented in section 2.1.2 Review of the grounding line mapping techniques of this thesis.

Figure 1-3 The grounding zone of Darwin Glacier (79°50' S, 159°50' E) (Floricioiu, 2016). In the background are the Transantarctic Mountains.

1.3 Research Objectives

There are several objectives in this study at different levels.

First, this study provides a summary of observations on short-term changes of the GLL derived from spaceborne SAR data and the variation of the ocean tide amplitude at specific selected sites in Antarctica. Additionally, information of other known factors affecting

GLL short term migration, such as bedrock topography and the corresponding slope, are provided for comparison.

Further, the study investigates whether there is any correlation between GLL properties and tidal motion. A qualitative description is given.

Depending on the complexity of the grounding line structure and the topography of the bedrock, statistical analysis of the derived changes in GLL is carried out, aiming to provide insights on the contribution of GLL migration by ocean tides.

Finally, the study tries to answer the question: To what extend should ocean tides be taken into consideration when quantifying GLL retreat due to ice thinning?

1.4 Thesis Outline

The theoretical background needed to understand this study is presented in Chapter 2. An introduction to the specific topics in earth system science is given, including glacier formation, grounding line, tidal cycle and atmospheric pressure. Further, the principles of the remote sensing technology used in this study, SAR and InSAR techniques as well as DInSAR GLL tracking methodology are explained.

Chapter 3 is dedicated to the SAR and auxiliary data needed to generate the GLL and to the workflow developed to investigate the GLL migration.

The results and analysis are presented in Chapter 4, followed by a discussion on the findings.

Chapter 5 rounds up and concludes the study, providing an outlook for future possible research directions.

CHAPTER 2
Background

2.1 Grounding line definition and retrieval techniques

2.1.1 Glaciological basics of processes at the grounding line

The mechanism of glacier formation, ice movement and groundline line migration are introduced in this section.

Glaciers form from precipitation, mainly snow, which are small grains of ice crystal with large air pockets between grains. When the snow accumulates on the ground, the weight of snow compresses itself into larger grains and reduces the size of air pockets. Over time, the crystal size keeps on increase, air pocket size decreases and the density increase, turning the snow into firn—an intermediate state between snow and glacier ice, and eventually into glacier ice- with crystal size up to inches and very tiny air pockets(Cuffey & Paterson, 2010, Chapter 2).

Glacier is moving slowly- as it is soft, in comparison to rock, and easily subject to deformation. There are various kinds of force acting the glaciers that would lead to movement: the gravity, the sheer force of glacial ice. In general, the movement of ice at the bottom is slower than the top due to the friction with the bedrock. The sliding of a glacier over a bedrock is referred as a basal slip (Cuffey & Paterson, 2010, Chapter 7).

Depending on the size, place of formation, properties, glacial ice is often given more specific names. For example, ice sheets are referring to continental glacial ice extending more than over 50,000 square kilometers; ice shelves are glacial extensions over the continental margin and float on the ocean, which are the focus of this study.

The part of ice that is attached to the bedrock, also known as grounded ice, is relatively static in vertical motion, flowing solely in the horizontal direction by hundreds to thousands of meters per year. On the other hand, the floating ice is additionally being influenced by the ocean tides. In order to reach a hydrostatic balance, the ice shelf is moving vertically along with the tidal motion.

The boundary between the grounded ice and the floating ice is called a *grounding line*. However, due to the elasticity of ice, there isn't a sharp transition from grounded ice to floating ice. In reality,

7

the transition can extend over several kilometers, which is called a *grounding zone* (Fricker et al., 2009).
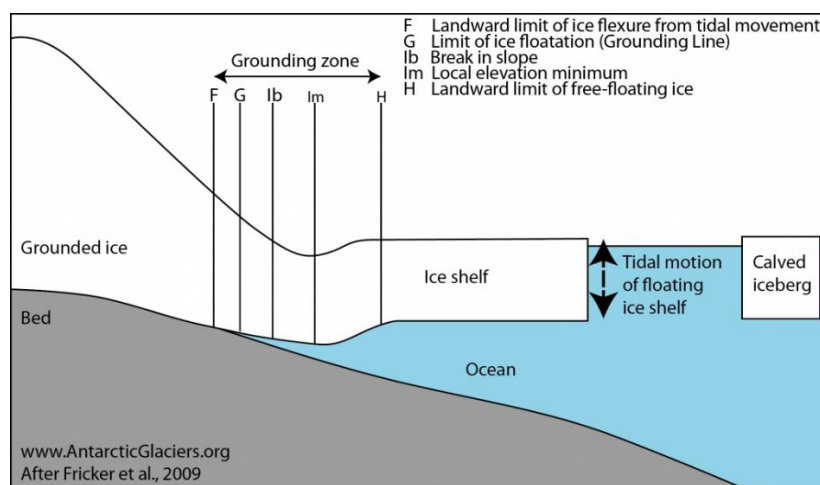
Figure 2-1 Features and processes at the grounding zone (adapted from Fricker et al., 2009).

Figure 2-1 shows schematically how a grounded ice transits to a floating ice, and typical features in a grounding zone (GZ). When the ice resting on bedrock detaches and becomes a floating ice shelf, a flexure in the transition area appears due to tidal motion affecting the floating part only (point **F** in Figure 2-1). **F** is also regarded as the landward limit of the grounding zone. Then, ice starts detaching from the bedrock (Point **G**). **I$_b$** is the break-in slope, the point of maximum curvature in ice flexure, which is in other words the most rapid change in surface slope. After the ice reaches its local minimum in elevation (Point **I$_m$**), the ice finally reaches hydrostatic balance (Point **H**), which is regarded as the seaward limit of the grounding zone. The exact distance between features points depends on ice thickness, Young's modulus for the ice, which is a function of the ice temperature profile, and also subglacial bedrock topography zone (Fricker et al., 2009). Moreover, the real grounding zone could be a complex-shaped structure instead of the one-dimensional transition shown in Figure 2-1.

2.1.2 Review of the grounding line mapping techniques

According to its definition, the GLL is located at point **G** in Figure 2-1 which is technically difficult to track. Thus, other features points in the grounding zone, serving as proxies of the true GLL, are detected. Table 2-1 summarizes the GLL products (Figure 2-2) generated from different GLL tracking techniques, which are now widely used by the scientific community. Although no product

has been released using in situ GPS and SARIn, these methods are included in Table 2-1, marking as the pioneer and the recent breakthrough of the development of GLL tracking.

Table 2-1 Overview of Antarctic wide GLL products.

Related Antarctic wide GLL products	Data type used	GZ features detected	Related publications
-	in situ GPS	F	(Riedel et al., 1999)
MOA	Visible satellite imagery from Terra/MODIS	I_b	(Scambos et al., 2007)
ASAID	Laser altimeter and visible satellite imagery from Landsat-7	I_b	(Bindschadler et al., 2011)
MEaSUREs, AIS CCI	SAR (DInSAR)	F	(Rignot et al., 2011) (DLR, 2018)
-	Radar altimeter (SARIn of Cryosat-2)	F, H, I_m, and I_b	(Dawson & Bamber, 2020)
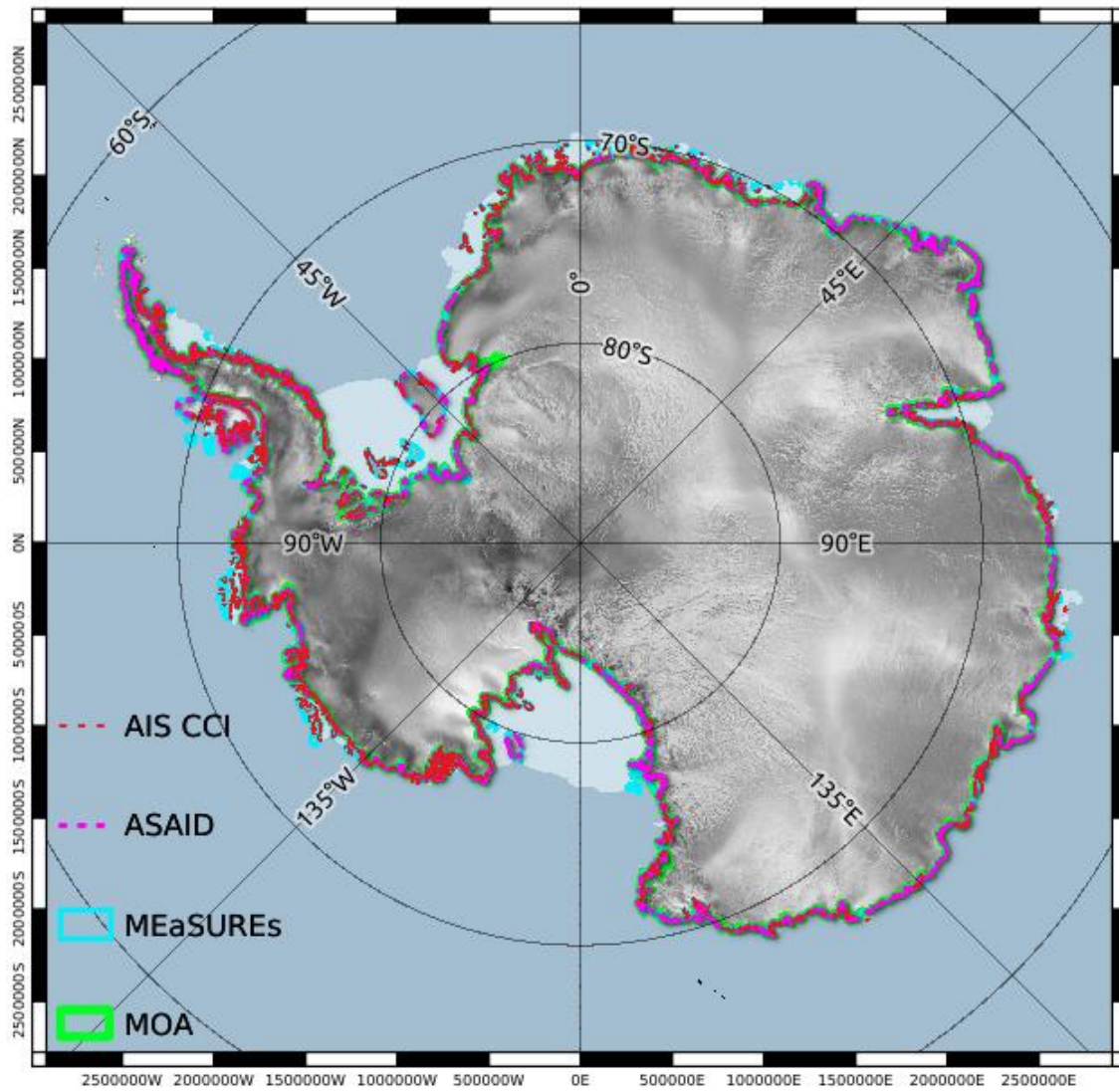
Figure 2-2 Antarctic wide GLL products overlaying over RAMP RADARSAT mosaic.
Generated from Quantarctica dataset (Roth et al., 2017).

In general, apart from the type of sensor used, GLL tracking techniques can be classified into 2 categories:

- The dynamic method is referring to detecting the vertical motion of GZ due to ocean tides.
- The static method is mapping the ice flexure from elevation information as a temporal snapshot.

In 1999, Riedel et al. presented field work using in situ GPS to investigate the response of grounding zone to tidal forcing. This study was carried out at the Ekström Ice Shelf in East

Antarctica. The emphasis of the study was to observe the horizontal and vertical components of the ice displacement, recorded by GPS equipment, across the GZ continuously. The study showed that it is possible to estimate the range of the ocean tides on the ice body and to derive the tidal deflection.

Scambos et al. released several Mosaic of Antarctica (MOA) data sets based on MODIS visible imagery in 2007. 260 MODIS images were assembled to form the mosaic for the Antarctic continent and surrounding islands. MOA surface morphology images, which provide information on topographic and albedo features, were used to extract among other parameters also the GLL. This manually delineated product corresponds to the slope break I_b, which is visible in the imagery due to brightness change.

Brunt et al. (2010) presented a technique for mapping the grounding zone at the Ross Ice Shelf, Antarctica using ICESat laser altimetry data. ICESat, crossing the GZ of Ross Ice Shelf at 491 locations, detected the ice flexure of the GZ as well as the short-term sea level changes induced by ocean tides. Considering the temporal changes in the ice surface elevation due to ocean tidal forces, by analyzing ICESat repeat-track data, the locations of the F, H, I_m, and I_b features points of the GZ were estimated.

As part of the Antarctic Surface Accumulation and Ice Discharge (ASAID) project, a high-resolution mapping product of groundline product based on Landsat-7 imagery and ICESat/GLAS laser altimetry was released by (Bindschadler et al., 2011). GLL were derived from laser altimetry data, which contains information about ice elevation change. ASAID GLL is most consistent with point I_b.

As a part of the NASA's MEaSUREs project, an Antarctic wide GLL product from double difference interferometry (DInSAR) was released in 2011 and updated in 2016 (Rignot et al., 2011). The same technique has been used also for the GLL product, developed within ESA's Antarctic Ice Sheet Climate Change Initiative (AIS_cci) project, by the German Aerospace Center (DLR). DInSAR is a dynamic method and makes use of the temporal changes of ice surface elevation. GZ appears as a close-packed fringe belt in a DInSAR interferogram. Details of DInSAR methodology are presented in section 2.2.3 DInSAR GLL tracking methodology, while details of the AIS_cci grounding line product are given in section 3.3 The AIS_cci GLL processor and products.

11

Dawson & Bamber (2020) have derived the GLL and GZ using elevation data acquired from CryoSat-2 SARIn mode. The SARIn mode combines delay-Doppler processing to improve along-track resolution, with dual antennas to provide the location of the return echo in the cross-track direction. Comparing to a conventional altimeter, the SARIn mode has overcome issues like off-ranging and loss of lock near break-in slope.

Among all techniques, DInSAR is considered as one of the most accurate methods in detecting and tracking the landward limit of ice flexure (**F** in Figure 2-1) which lies very close to the GLL, **G**. While InSAR technique already has a wide range of glaciological applications, e.g. observing glacier motion and measuring ice-flow velocities, potential for further investigation is still found in DInSAR measurements. For example, it contains additional information on ice-shelf thickness, material properties and ocean tides. In combination with numerical modeling of grounding-zone flexure, it can be used to estimate ice-thickness distribution (Wild et al., 2018).

2.2 Synthetic Aperture Radar (SAR)

2.2.1 Basic SAR Principle

Radar (radio detection and ranging) is an active, microwave remote sensing system. It transmits high-frequency electronics in the microwave bands and receives the echoes from the scattering objects on the ground. Comparing to a passive, optical sensor, a radar has the advantages of being independent from illumination, meaning it has the capability to operate in both day and night. As the microwave bands are at the atmospheric absorption window, the pulse can mainly penetrate atmosphere and clouds, even partially penetrating vegetation, soil, snow and ice, depending on wavelength of choice.

A radar has a side-looking geometry, with azimuth direction along the flight direction (along-track-direction) and the range direction (cross-track-direction) along the Line-of-Sight (LOS). After image formation, the radar echoes are resolved into a 2-dimensional image in range-azimuth coordinates (Rosen et al., 2000). A radar image is complex because both amplitude and phase information are stored. In a radar image, the positions of targets are determined by slant-range distances, which are measured by the round-trip travel times between transmitted signals and backscattered signals from ground targets. Amplitude of returned wave energy, which is represented by the bright regions in a radar image, depends on the surface slope, roughness, and

the dielectric characteristics of the surface material while the phase is a term proportional to the range to the target (Bürgmann et al., 2000).
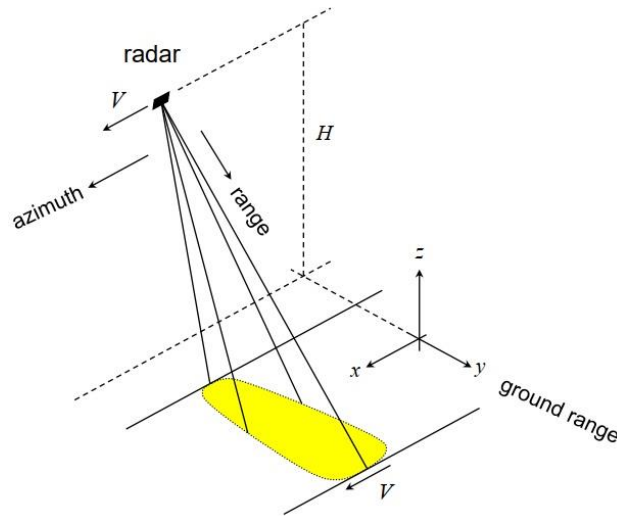
Figure 2-3 Radar Side-Looking Radar Geometry (adapted from Bamler, 2000).

The motivation of developing a synthetic aperture radar (SAR) is that the azimuth resolution of a conventional radar, or also known as real aperture radar (RAR), is physically constrained by the equation (Moreira et al., 2013):

$$\delta_a = \frac{R\lambda}{D} \qquad (2.1)$$

In order to achieve higher azimuth resolution δ_a, which is given by the smallest separation between two points targets that can be detected by the radar, one would like to reduce the wavelength λ of transmitter, or to reduce range R of sensing, or to use an antenna with a larger aperture D. Every option has its own limitation: the choice of wavelength is limited by electromagnetic properties; the nature of mission (spaceborne/ airborne) has limited the minimum possible range; building a large antenna increases the cost of the mission. A spaceborne RAR would have a resolution of about 5–10 km and thus would be of little use for practical earth remote sensing applications (Bürgmann et al., 2000).

A large 'synthetic antenna' is formed by combining signal processing techniques with satellite orbit information. By focusing the raw radar echoes, SAR processing produces a much-higher-resolution

13

radar image in both cross-track and along-rack direction, with a typical image point (pixel) spacing in spaceborne SAR images of 20–100 m within a 100-km-wide swath (Bürgmann et al., 2000).

In along-track direction, making use of the fact that the radar transmits pulse and receive echoes at a regular pulse repetition frequency (PRF), the returning echoes corresponding to consecutive pulses are processed as if they originated from an array of antennas distributed along the radar's flight path. While the antenna is in motion, the Doppler frequency shift of the return signal depends on whether the location of the target is fore or aft of the radar beam's center, thus is used together with the round-trip time of the signal to differentiate image points in the azimuth direction. In cross-track direction, differentiation of radar echoes from closely spaced targets can be improved by using a radar signal of high bandwidth (Bürgmann et al., 2000).

With the formation of a 'synthetic antenna', the azimuth resolution is no longer limited by equation (2.1). There is also possibility for SAR missions to alternate between different imaging modes, depending on the requirement of resolution of the mission. Related information is outlined in section 3.1 The Sentinel-1SAR Mission.

However, in conventional SAR imaging, the interpretation of the radar image is adversely affected by the altitude-dependent distortion. In a slant-range, a target with a higher elevation is closer to the radar. Figure 2-4 shows how a mountainous terrain is distorted on a radar image. The phenomenon that slopes facing towards the radar appearing shortened are known to be 'foreshortening'; Steep slopes might be superimposed to adjoining sections of the scene, range-bins order might even be inverted - known as 'layover'. Data in layover zones are ambiguous and cannot be used for quantitative analysis; Back-slopes which are not illuminated by SAR cast 'shadows' on the radar image, since there is no returned signal (Richards et al., 2010; Rott, 2009).
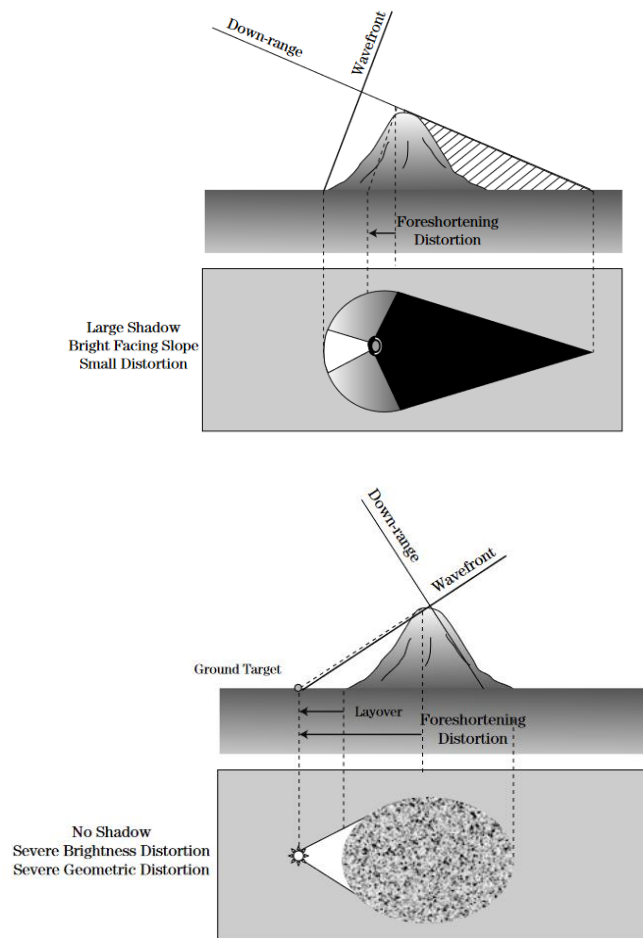
Figure 2-4 Distortions of position on a radar image (Richards et al., 2010). Left: Foreshortening and shadow; Right: Layover.

SAR imaging collapses the three-dimensional world to two-dimensional images, yet the development of InSAR techniques enables measurement of the third dimension.

2.2.2 SAR Interferometry (InSAR)

In this section, the principle of InSAR will be outlined with an emphasis on repeat-pass interferometry.

The idea of InSAR is to consider the phase difference between complex SAR data acquisitions in the same imaging geometry with precise co-registration, thus producing an interferogram (Rott, 2009). Interferometry with SAR images acquired by one radar at different time is known as 'repeat-pass InSAR', while interferometry with SAR images acquired by multiple antennas at the same

time is referred as 'single-pass InSAR'. The various InSAR techniques differentiate also by the exploited baseline type. Figure 2-5 illustrates the geometry of a cross-track InSAR acquisition, when the SAR sensors are imaging the same surface at the same time but at slightly different geometries. This is given by the sensing position of the 2 SARs with mutually displaced flight tracks, separated in space by the baseline B, with a component perpendicular to the LOS as the effective baseline $B_\perp$(Bamler et al., 2003). On the contrary, an along-track InSAR, acquires data from the same flight track but at different times (Moreira et al., 2013), thus it is a kind of repeat-pass InSAR. Cross-track interferometry is used for generating digital elevation models (DEM). In repeat-pass InSAR, the temporal baseline, ranging from seconds/minutes to days up to years, dictates the potential applications. Repeat-pass InSAR is used for measuring land deformation or surface movement.

Although sometimes along-track InSAR is named 'differential interferometry', and thus given the abbreviation 'DInSAR', it is important to note that the definition of this abbreviation is not used in this thesis (further explanation in the next section 2.2.3 DInSAR GLL tracking methodology).
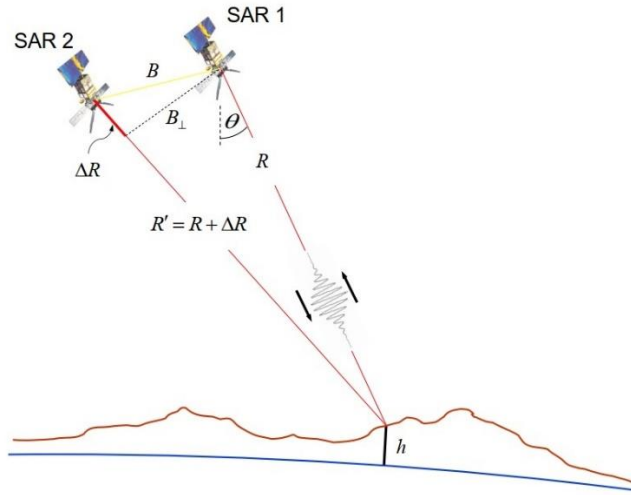
Figure 2-5 Cross-track InSAR configuration (adapted from Bamler et al., 2003). The flight paths of SAR 1 and SAR 2 are perpendicular to the plane of the drawing.

For each pair of corresponding image points, the phase difference, also known as the interferometric phase $\Delta\phi$, is related to the propagation path difference ΔR of the 2 radar beams:

$$\Delta\phi = \phi_2 - \phi_1 = -\frac{4\pi}{\lambda}\Delta R \qquad (2.2)$$

Depending on the type of baseline, the weighting of contributions to $\Delta\phi$ are different. For repeat-pass InSAR, $\Delta\phi$ is made up by the following contributions:

$$\Delta\phi = \Delta\phi_{flat} + \Delta\phi_{topo} + \Delta\phi_{dis} + \Delta\phi_{atm} \qquad (2.3)$$

Where $\Delta\phi_{flat}$ and $\Delta\phi_{topo}$ are caused by the relative radar-target distance changes for flat earth and topography; $\Delta\phi_{dis}$ is by cause of the displacement of the observed surface element in LOS, e.g. ice shelf movement due to tidal motion; $\Delta\phi_{atm}$ is mainly due to changes in the water vapour content of the atmosphere (Rott, 2009, Hanssen et al., 2001). The flat earth phase has usually been eliminated in the interferometric processing if precise data of the radar position, e.g. satellite orbit data, is known. $\Delta\phi_{atm}$ is unfavorable for quantitative analysis and thus is considered as an error source.

Despite its powerfulness, the InSAR technique is vulnerable to decorrelation and phase errors, which at times leads to lack of phase coherence and in consequence unusable interferograms. Besides changes in atmospheric water vapour content, a major limitation of repeat-pass InSAR is the temporal decorrelation (Rott, 2009). Stability of the scattering properties of a target is essential when forming an interferogram. The region of image becomes incoherent when the scattering properties of a target changes in time, e.g. the change of a scattering snow surface due to melting, or individual scatters within the same pixel moving relative to each other, e.g. wind-induced motion of a vegetation canopy. In addition to above, InSAR is also affected by other error sources, including phase noises originating from radar system and processor, source DEM errors, baseline error and data gaps due to image distortion (layover, shadow) (Bürgmann et al., 2000).

2.2.3 DInSAR GLL tracking methodology

DInSAR is referring to double difference interferometry. The use of repeat-pass DInSAR to detect GZ was first proposed by Rignot in 1996 . This method makes use of the temporal changes of ice surface elevation. GZ appears as close-packed fringe patterns on a DInSAR interferogram.

In order to generate a DInSAR interferogram, SAR images of minimum 3 consecutive repeat passes or 2 repeat-pass pairs of the same relative orbit are used to generate two independent interferograms. One should note that, although images of the same relative orbit are chosen, there may still be aslight difference in acquisition position of antenna. In other words, topographic contribution of phase may not be completely eliminated by just taking the difference.
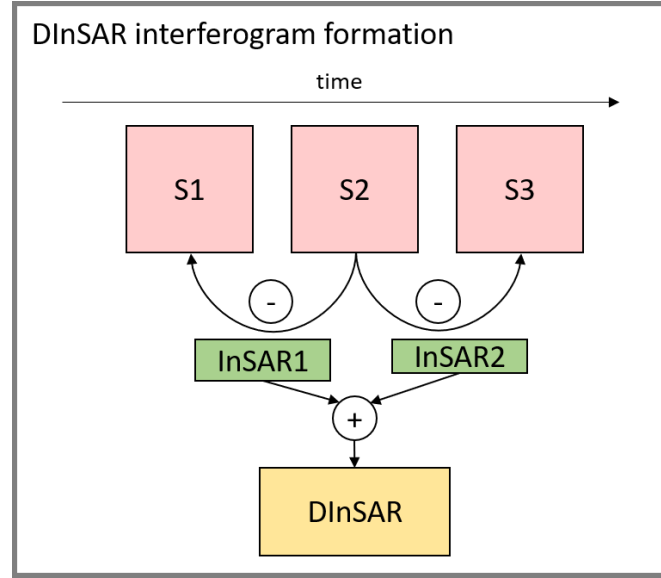
Figure 2-6 DInSAR interferogram formation from SAR triplet.

Figure 2-6 shows the formation for a DInSAR interferogram from three consecutive repeat pass SAR acquisitions (SAR triplet). As the first step, 2 interferograms between 1st & 2nd and 2nd & 3rd SAR image are generated, which the interferometric phases of pixels equal to:

$$\phi_{12} = \phi_2 - \phi_1$$
$$\phi_{32} = \phi_2 - \phi_3 \tag{2.4}$$

The phase contribution in equation (2.3) in a scenario of observing tidal deflection of ice shelf is specified as below (assumed $\Delta\phi_{\text{flat}}$ has been eliminated):

Table 2-2 Phase contribution in an interferogram observing tidal deflection of ice shelf.

ϕ_{12}	ϕ_{32}
Topography (due to antenna position difference)	Topography (due to antenna position difference)
Ice LOS motion (+)	Ice LOS motion (-)
Elevation difference due to tidal motion between t_1 and t_2	Elevation difference due to tidal motion between t_3 and t_2
Atmospheric condition difference between t_1 and t_2	Atmospheric condition difference between t_3 and t_2

For the purpose of GLL determination, the atmospheric condition term is assumed to be neglectable, since water vapor changes in atmosphere occur at a much large spatial scale in

comparison with GLL variation. Therefore, the error contribution would not affect GLL determination.

Assuming the ice LOS motion is almost constant, the phase of the 2 interferograms are added to eliminate the ice LOS motion term. A surface elevation DEM is used to remove the topographic phase contribution in both interferograms. Finally, a DInSAR interferogram that depends solely on the tidal displacements is retrieved:

$$\phi_{12,flat} + \phi_{32,flat} = C(Z_2 - 0.5(Z_3 + Z_1)) \qquad (2.5)$$

Where C is a constant related to the wavelength and incidence angle of the radar, and $Z_2 - 0.5(Z_3 + Z_1)$ is the relative tidal displacement between scene 2 and the average of scene 1 and scene 3. Figure 2-7 shows an example from (Chowdhury et al., 2016) of how horizontal ice flow is cancelled in a double difference interferogram. The expected GLL is annotated with a red line.
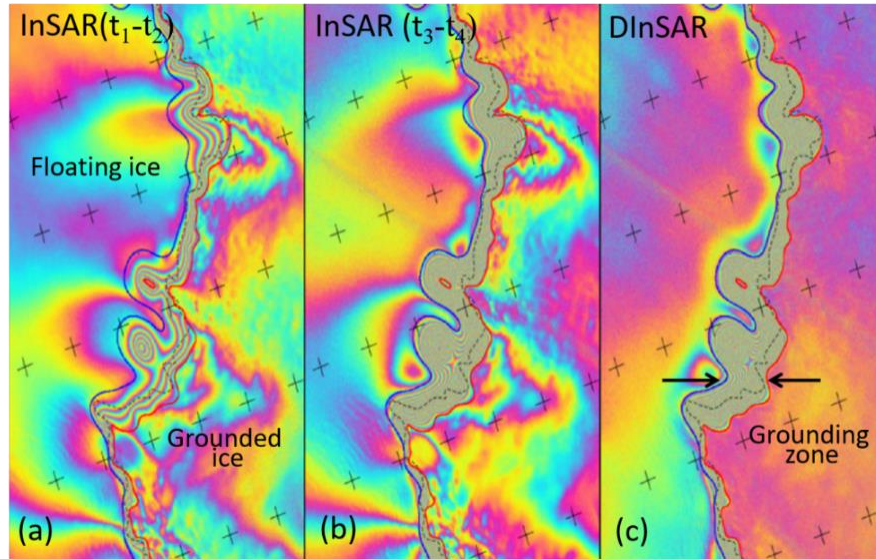
Figure 2-7 Example of DInSAR formation: (a) and (b) the two single interferograms and (c) the resulting double difference interferogram (Chowdhury et al., 2016).

2.3 Ocean Tides

Tides are the changes in sea levels caused by the gravitational forces and the rotation of the Earth. According to Newton's law of universal gravitation, the gravitational force between two bodies is directly proportional to the mass and inversely proportional to the square of distance. The moon causes the strongest gravitational pull because it is the closest celestial body to Earth. A tidal bulge

would form along the Earth-Moon axis, not only the near moon side but also the far-side due to inertia (Ross, 1995). Though far from Earth, the sun has the second strongest gravitational pull on earth, which is about half that of the moon (Thurman, 1997), due to its huge mass.

Over time, the relative positions to the Earth's equator of these celestial bodies change, causing changes to daily tidal heights in locations. In each lunar month, two sets of spring tides and two sets of neap tides occur (Figure 2-8) (Sumich & Morrissey, 2004). Spring tides happens when the Sun, Moon, and Earth are in alignment, which causes increasing tidal range. Neap tides happen when the Earth-Moon axis is perpendicular to the Earth-Sun axis, which produce moderate tides.
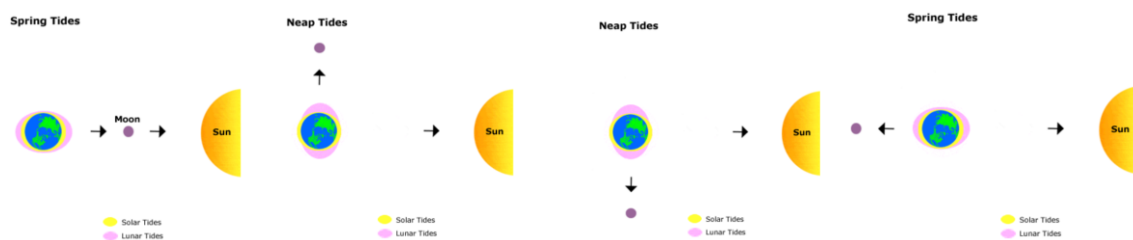

Figure 2-8 Spring tides and neap tides (adapted from US Department of Commerce, n.d.).

Tidal range is also affected by the Earth-Moon distance and Earth-Sun distance. In one lunar month, the tide range is greater than average when the Moon is at the perigee and the tide range is smaller than average when the Moon is at the apogee. Similarly, in each calendar year, the tide range are enhanced when the Earth is at the perihelion and the tide range reduced when the Earth is at the aphelion (Thurman, 1997).

The continental interference contributes to complex tidal pattern in different ocean basins. If there was no land, every location on the globe should experience two high tides and two low tides every lunar day (Ross, 1995) due to the rotation of the Earth. However, the existence of large continents has blocked the westward passage of the tidal bulges as the Earth rotates. In result, different tidal patterns are induced in different coastline. In general, there are 3 types of tide cycles:

- Semidiurnal tides: Experiencing two high tides and two low tides every lunar day with approximately equal size. Common on the eastern coast of North America and Africa.
- Mixed Semidiurnal tides: Experiencing two high tides and two low tides every lunar day with different size. Common on the western coast of North America.
- Diurnal tides: Experiencing one high tide and one low tide every lunar day. Could be found in Gulf of Mexico.

In addition, atmospheric conditions also affect tides. According to an empirical study conducted by (Padman et al., 2003), a difference from the standard barometric pressure (1013.25 hPa) of 1 hPa can cause a difference in height of 1 cm.

In order to observe tides, tide gauges and satellite altimetry techniques have been used for tidal observation and provided valuable data for understanding the tide patterns. Although numerous field measurements of ocean tides have been done globally, getting an accurate knowledge of the tides in Antarctica is particularly difficult, due to the shortage of tide gauges on the continent and the blockage of useful altimetric measurement by sea ice (Oreiro et al., 2013).

Therefore, globally and particularly in Antarctica one has to rely on models for estimating and predicting tide level. Tide models are designated for different spatial coverage. For example, TPXO provides a series of fully-global models of ocean tides (Egbert & Erofeeva, 2002), while the Circum-Antarctic Tidal Simulation (CATS2008) is a high-resolution regional inverse model of the entire circum-Antarctic ocean developed by (Padman et al., 2002). CATS2008 simulations include ocean cavities under the floating ice shelves, coastline and grounding lines, water depth map all these being specific features for Antarctica.

Most tide models estimate the tide levels under standard barometric pressure. To include the effect of atmospheric pressure (P in Pa), a corrected tide level is computed as follow:

$$Tide_{corrected} = Tide_{modelled} - \frac{101325 - P}{g\rho_{seawater}}$$ (2.6)

Where g is the gravity constant and $\rho_{seawater}$ is the density of seawater, assumed to be $1026.0 \; kg/m^3$.

Oreiro et al. (2013) has carried out a comparison of different tide models using data from satellite altimeters and tide gauges in the northeast sector of the Antarctic Peninsula. Figure 2-9 shows that CATS2008 has the lowest Residual Sum of Squares (RSS) value, which is obtained from the Root Mean Square (RMS) misfit of the 8 tidal constituents using the following equation:

$$RSS = \sqrt{\sum_{j=1}^{M} RMS_j^2}$$ (2.6)

indicating CATS2008's capability to match with tidal observation in Antarctica.
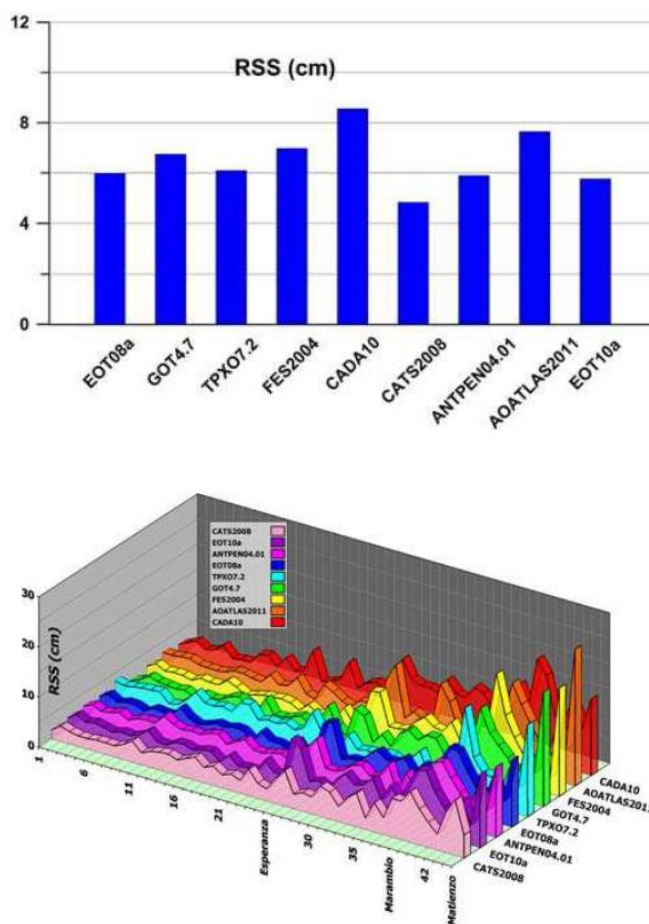
Figure 2-9 Comparison of the RSS obtained for various tide models. Above: at individual locations. Bottom: at whole investigated area (Oreiro et al., 2013).

CHAPTER 3
Data and Processing

Chapter 3 is dedicated to data and the developed processing used in the present study. Input data, highlighting to the SAR missions and the AIS_cci grounding line processor, and newly developed processing steps are introduced in corresponding sections in this chapter.

3.1 The Sentinel-1SAR Mission

Sentinel-1 is a radar imaging mission for ocean, land and emergency services. It is the first of the five missions developed for the Copernicus Programme by the European Space Agency (ESA). The Copernicus Programme aims to integrate and provide comprehensive information for operational monitoring of the environment and for civil security.

The mission comprises currently a constellation of two satellites, Sentinel-1A and Sentinel-1B, each carrying one C-band SAR instrument onboard. The two satellites are flying 180 deg apart on the same near-polar sun-synchronous orbit plane at the height of 698 km (Figure 3-1). While the orbit ground track itself has a 12-day repeat cycle (Table 3-1), the Sentinel-1 constellation is able to achieve a 6-day repeat cycle (Torres et al., 2012).

Table 3-1 Sentinel-1 Orbit Information (Torres et al., 2012).

Altitude	693 km
Inclination	98.18 deg
Period	98.6 min
Repeat Cycle	12 days
Ref. tube deviation	±100 m
Local Time at Ascending Node	18:00 hours
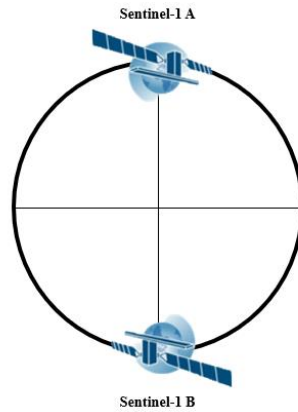
Figure 3-1 Sentinel-1 constellation (adapted from ESA, 2013).

Sentinel-1 SAR can be operated in 4 exclusive imaging modes (Figure 3-2) with different resolutions and coverage: Interferometric Wide Swath Mode (IW), Extra Wide Swath Mode (EW), Wave Mode (WV) and Stripmap Mode (SM). In this study, repeat-pass Sentinel-1 data acquired in IW mode were used for DInSAR grounding line processing.

The IW mode allows combining a large swath width (250 km) with a high geometric resolution (5 m $\times$ 20 m on ground). Interferometry is ensured through sufficient overlap of the Doppler spectrum (in the azimuth domain) and the wave number spectrum (in the elevation domain). Using the Terrain Observation by Progressive Scan (TOPSAR) operation, the IW mode harmonizes the performance in along-track direction and reduces scalloping (Torres et al., 2012).

Figure 3-2 Sentinel-1 operational modes (Torres et al., 2012).

24

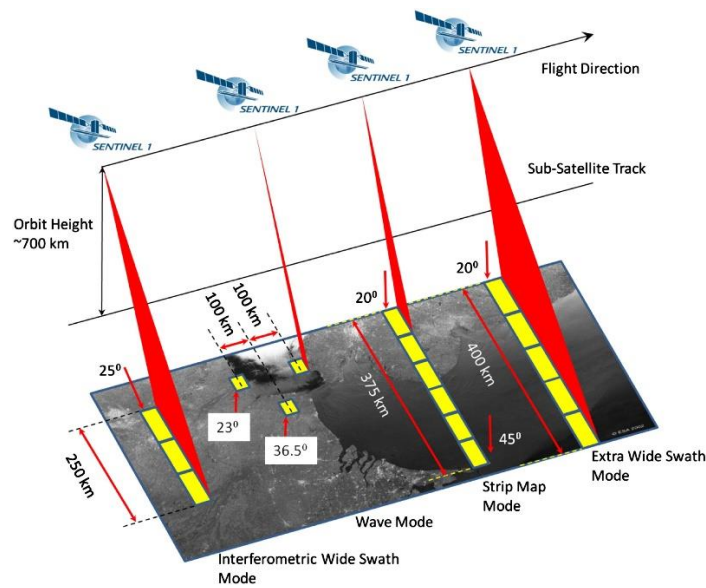## 3.2 The TanDEM-X SAR mission and the global DEM

TanDEM-X stands for 'TerraSAR-X add-on for Digital Elevation Measurement' and consists of two twin satellites, which both has an X-band SAR on board. The main goal of the TanDEM-X mission was the generation of world-wide, consistent, timely, and high precision digital elevation models according to the HRTI/DTED-3 (12 m posting, 2 m relative height accuracy) standard as the basis for a wide range of scientific research (Krieger et al., 2007).

Flying in a close formation, the 2 satellites act as a single-pass SAR interferometer with the opportunity for flexible baseline selection. This enables the acquisition of highly accurate cross- and along-track interferograms without the inherent accuracy limitations imposed by repeat-pass interferometry due to temporal decorrelation and atmospheric disturbances (Krieger et al., 2007).

For operational DEM generation, the TanDEM-X satellites are flying in HELIX formation (Figure 3-3). Combining a horizontal (out-of-plane) orbital displacement by different ascending nodes with vertical (radial) separation by different eccentricity vectors, the formation results in a helix-like relative movement of the satellites along the orbit. The formation allows arbitrary shifts of satellites along their orbits avoiding crossing of orbits, which enables a safe spacecraft operation (Krieger et al., 2007).
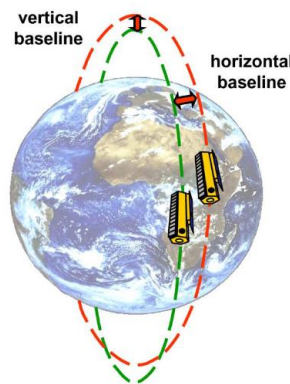

Figure 3-3 HELIX satellite formation for TanDEM-X (Krieger et al., 2007).

In this study, the 90m global DEM product generated from single pass TanDEM-X data acquired between 2010 and 2015, provided by the EOC Geoservice of the Earth Observation Center (EOC) of DLR, was used for the topographic correction of the DInSAR GLL processing. The DEM has a

25

reduced pixel spacing of 3 arcseconds (90m at the equator) and covers all landmasses from pole to pole (DLR, n.d.).

3.3 The AIS_cci GLL processor and products

For the present study the GLL products ofthe AIS_cci project (https://climate.esa.int/en/projects/ice-sheets-antarctic/) were used. The workflow of the AIS_cci GLL processor is shown in Figure 3-4.
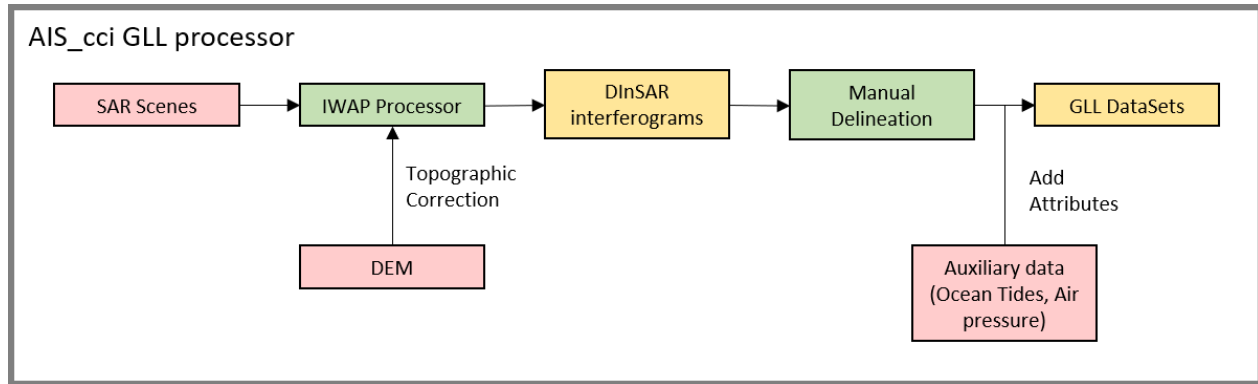
Figure 3-4 AIS_cci GLL processor: input Data (pink), processing modules (green) and output data (yellow).

DInSAR interferograms are generated from repeat pass SAR data by DLR's Integrated Wide Area Processor (IWAP) (Gonzalez et al., 2013), with topographic correction according to a DEM. After the generation of the DInSAR interferogram, the GLL is delineated manually along the landward limit of the dense fringe belt and saved in the AIS_cci GLL product data format.

AIS_cci GLL products (Thorvaldsen, 2017) are delivered in the ESRI Shapefile data format, in the reference system and projection namely WGS 84 Antarctic Polar Stereographic, EPSG:3031. Useful information for analysis is stored in the product attribute table, including time of SAR data acquisitions and the corresponding ocean tide levels and air pressure. Table 3-2 highlights some of the attributes that are important for the analysis of this study.

Table 3-2 Selected attributes annotated in the AIS_cci GLL product relevant for this study (adapted from Thorvaldsen, 2018).

Attribute Name	Explanation
T1	UTC Datetime string of pass 1
T2	UTC Datetime string of pass 2
T3	UTC Datetime string of pass 3
RP_LON	Longitude (WGS84) of reference point for tide/air pressure extraction
RP_LAT	Latitude (WGS84) of reference point for tide/air pressure extraction
COR_OTL_T1	air pressure corrected ocean tide level at (RP_LON, RP_LAT) at T1 in meter
COR_OTL_T2	air press. corr. ocean tide level at (RP_LON, RP_LAT) at T2 in meter
COR_OTL_T3	air press. corr. ocean tide level at (RP_LON, RP_LAT) at T3 in meter
DH1	expected vertical difference 1 [m]: DH1 = COR_OTL_T2– COR_OTL_T1
DH2	expected vertical difference 2 [m]: if (num_passes == 3): DH2= COR_OTL_T2- COR_OTL_T3
DHF	final height difference [m] if num_passes == 3: DHF = DH2+ DH1

3.4 Additional data: air pressure from NCEP reanalysis and the subglacial topography from BEDMAP2 DEM

The National Centers for Environmental Prediction (NCEP) Reanalysis is a NOAA project using a state-of-the art analysis/ forecast system to perform data assimilation using past data from 1948 to the present (Kalnay et al., 1996). In this study, NCEP air pressure reanalysis data were used to correct modelled tide levels (i.e. COR_OTL_Tn attributes in Table 3-2) resulted from CATS2008 (section 2.3 Ocean Tides).

BEDMAP2 is a suite of ice surface elevation, ice thickness and subglacial topography datasets for Antarctica up to 60°S (Fretwell et al., 2013). The BEDMAP2 products were derived from data of a variety of sources. In this study, the bedrock DEM (Figure 3-5), which has a spatial resolution of 1km, was used to complement the GLL migration analysis.
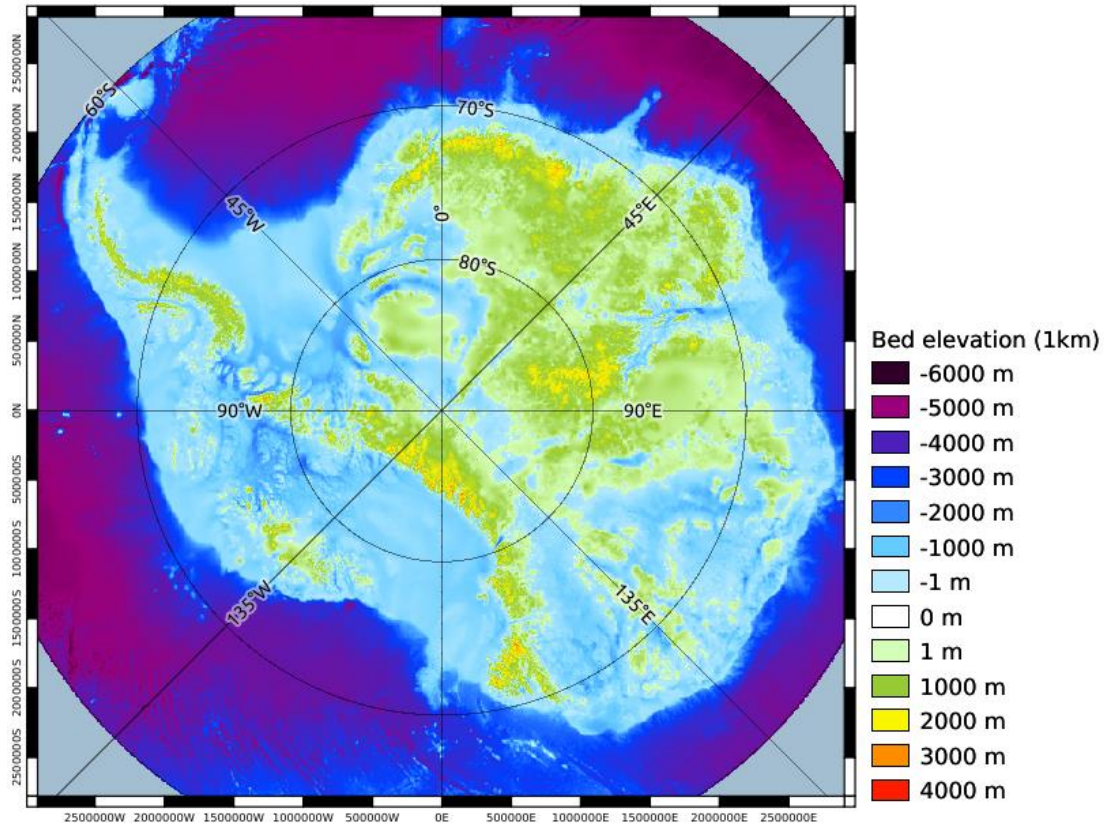
Figure 3-5 BEDMAP2 Bed Elevation at 1km resolution. Generated from Quantarctica Dataset (Roth et al., 2017)

3.5 Overall workflow for GLL migration

As a summary, the schematic diagram (Figure 3-6) shows the workflow of this study which comprises 3 major processing components: GLL processing, Tide processing and GLL time series analysis.

28
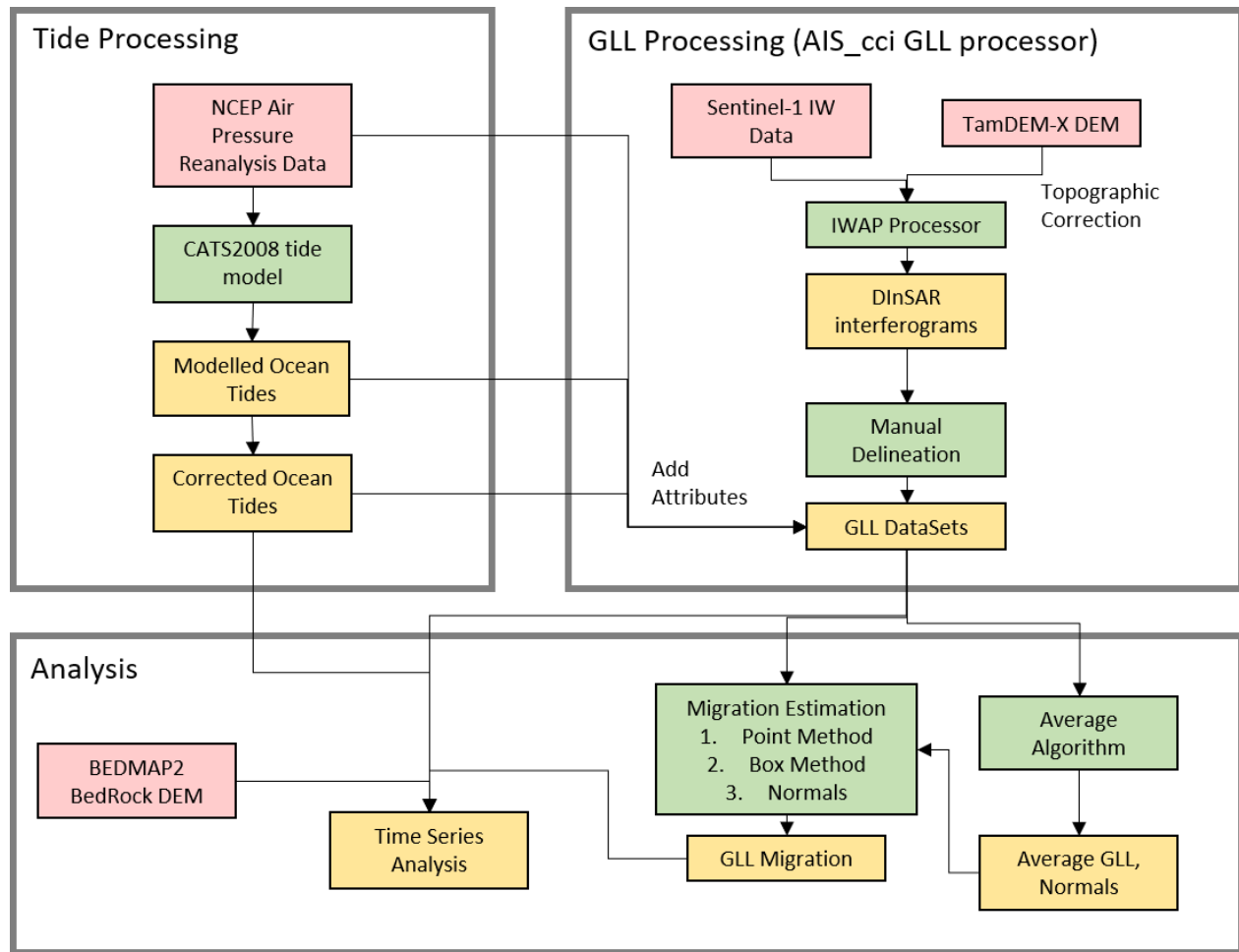
Figure 3-6 Overview of the data and processing steps for GLL migration analysis: input data (pink), processing modules (green) and output data (yellow)

The GLL processing, which mainly takes place in the AIS_cci GLL processor, has been described in section 3.3 The AIS_cci GLL processor and products. As mentioned in the sections 3.1 The Sentinel-1SAR Mission and 3.2 The TanDEM-X SAR mission and the global DEM, Sentinel-1 data acquired in IW mode was used as input SAR scenes (the choice of scenes is further elaborated in Figure 4-1 and Table 4-1) and the 90m global TanDEM-X DEM product data was used for the topographic correction of the DInSAR GLL processing.

For tide processing, CATS2008 (section 2.3 Ocean Tides) was used to model ocean tide level corresponding to time and location of scenes, following by atmospheric pressure correction according to NCEP air pressure data and equation (2.6). Beside annotating GLL products (as

mentioned in section 3.3 The AIS_cci GLL processor and products), the corrected ocean tides were also used in the GLL time series analysis.

As a prerequisite to the GLL migration analysis, an average GLL had to be generated as a reference line. Novel algorithms for averaging GLL datasets and computing migration are introduced in the sections 3.6.1 Reference GLL generation and 3.6.2 GLL migration , respectively.

The time series analysis was performed to investigate whether there is any correlation between GLL geometric properties (e.g. the fringe density) and migration extent, and the ocean tide level and bedrock topography from BEDMAP2.

3.6 Algorithms for GLL migration and average GLL

In order to analyze short time series of GLLs, two procedures were developed within this study. The first algorithm refers to an averaged GLL needed as reference and the second one is related to computing the GLL migration.

3.6.1 Reference GLL generation

Instead of using current existing external GLL datasets (Table 2-1), a suited average GLL is needed as reference for the multi temporal Sentinel-1 GLL dataset, ensuring the reference GLL is representative for the corresponding acquisition period of the satellite data and methodology applied to obtain the GLL dataset.

The workflow for the generation of the average GLL is shown in Figure 3-7 and examples of the intermediate processing steps are illustrated in section 4.1 GLL Datasets, Migration and Average.
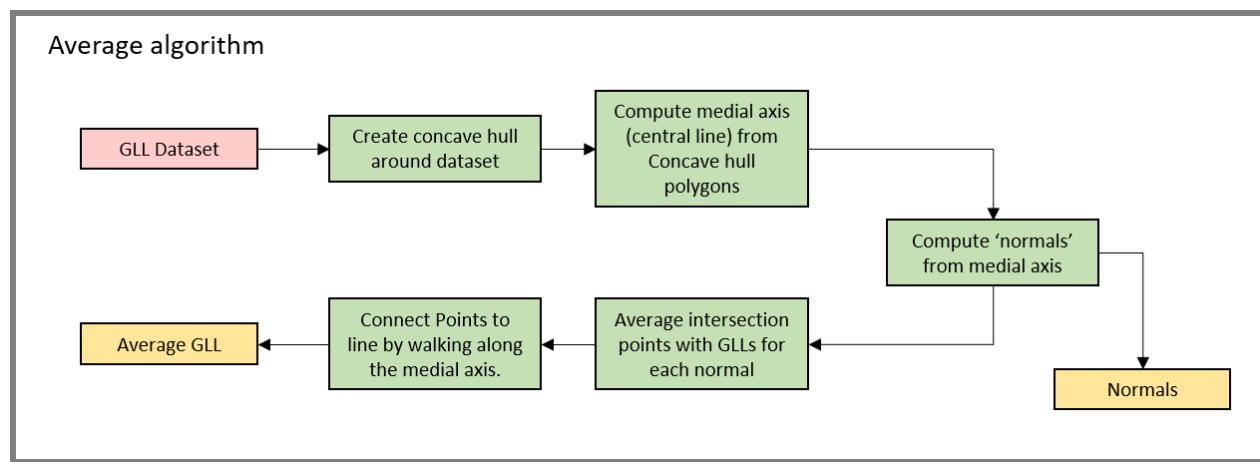

30

Figure 3-7 Flowchart of the GLL average calculation using as input data time series of GLLs (pink).

First, a concave hull polygon, or in general a polygon that closely encloses the GLL dataset, was created. Then, a medial axis was approximated based on the straight skeleton of the polygon. Normal lines along the medial axis with equal spacing were computed, intersecting nearby GLL segment. Ideally, the normal should not intersect other part of the GLL. The diagram (Figure 3-8) illustrates how a normal is computed from an arbitrary line (black curve).
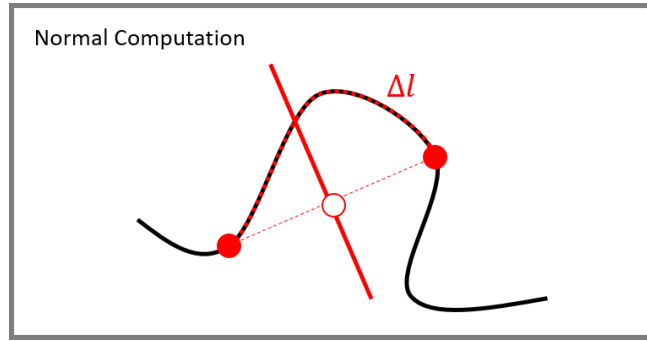
Figure 3-8 General approach to compute a normal (red line) to a curve (black line). With a line segment (red-black dotted line) with manually assigned length Δl on an arbitrary curve, the normal is perpendicular to and passing through the mid-point (white dot) of the shortest distance between the start-end points (red dots) of the line segment.

Next, considering the intersection points between each normal and the GLL datasets, the average GLL was created by connecting the centroids (average point) of the intersection points of each normal, along the medial axis. The average GLL served as reference in the computation of GLL migration. In addition, the normal was also used in GLL migration calculation.

In section 4.1 GLL Datasets, Migration and Average, the result generated in each step is presented. The effect of Δl on the algorithm performance and possible problem regarding multiple intersections of normal and GLL is discussed.

31

3.6.2 GLL migration

Figure 3-9 Three methods to compute the GLL migration between the neighbor GLL (orange line) and the reference GLL (black 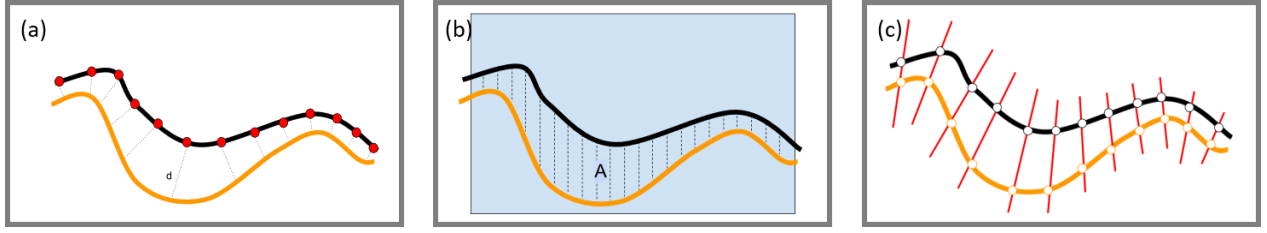line). (a) the point-line method, with neighbor GLL transforming to equally distanced points (red dots), d is the distance from point to reference GLL. and (b) box method, the 2 GLLs are bounded by a bounding box (blue box), separating with an area A. (c) Intersection (normal) method, the normal (red lines) are intersecting the 2 GLLs (white dots).

To quantify the short term GLL migration due to ocean tides, three methods were tackled: (Figure 3-9):

(a) The point-line method calculates the distance d from the equally distanced points on the neighbor GLL to the reference GLL. The migration $\bar{d}$ is computed by averaging d_n of the n points.:

$$\bar{d} = \frac{1}{n} \sum_1^n d_n \qquad (3.1)$$

(b) The box method considers the area A between the neighbor GLL and the reference GLL bounded by a bounding box, the migration is defined as:

$$\bar{d} = \frac{A}{\frac{1}{2}(L_1 + L_2)} \qquad (3.2)$$

where L_1, L_2 are the length of the 2 GLLs.

(c) The intersection method uses the normal lines generated from the averaging algorithm (Figure 3-8, red lines in Figure 3-9c). The distance $d_{n,l}$ between the reference GLL and a neighbor GLL (n) along a normal line (l) is measured. Applying equation (3.3), the migration $\bar{d}$ was computed

32

by averaging $d_{n,l}$ of all N possible normal-GLL combination. In addition, localize migration was estimated by considering a single normal.

$$\bar{d} = \frac{1}{N}\sum\nolimits^{n,l} d_{n,l} \tag{3.3}$$

For each method, the following 3 length-weighted average parameters were computed: mean migration, maximum migration and migration from average.

Table 3-3 GLL Migration parameters.

Mean Migration	The length-weighted average migration of all possible combinations in the GLL dataset.
Maximum Migration	The length-weighted average of the maximum migration of each GLL in the dataset.
Migration from Average	The length-weighted average of migration of GLLs in dataset from the reference GLL.

CHAPTER 4
Results and Analysis

4.1 GLL Datasets, Migration and Average

The study area for this experiment is located at key glaciers in Antarctica, mainly at Evans Glacier (78.3°S, 76.1°W) flowing into the Ronne Ice Shelf. They were selected based on the availability and quality of SAR scenes, observation of significant GLL migration and extent of tidal amplitude. Table 4-1 and Figure 4-1 show details and ground coverage of Sentinel-1 scenes used in this analysis. Every 3 consecutive scenes, with same relative orbit and slice number, were used for generating interferograms as shown in Figure 2-6 with methodology described in section 2.2.3 DInSAR GLL tracking methodology. Due to decorrelation and computational capacity, only interferograms of February, March and October were used for further analysis.

Table 4-1 Information of Sentinel-1 scenes.

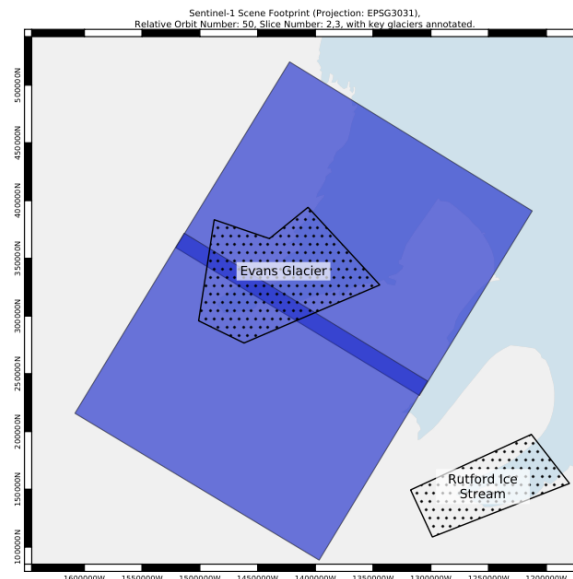|	
Product Type	Single Look Complex (SLC)
Year of acquisition	2020
Relative Orbit Number	50
Slice Number	2,3

Figure 4-1 Sentinel-1 footprint with key glaciers annotated.

Figure 4-2(a) shows a typical GZ feature on an DInSAR interferogram. The GZ appears as a dense fringe belt on the interferogram. With a priori knowledge on the geographic location, which eastward (right-side) of the belt is land and westward (left-side) of the belt is sea, the GLL was delineated along the landward limit of the belt. However, often the landward limit was not that trivial to be deduced. Figure 4-2(b) and (c) show examples of complicated GZ features. In Figure 4-2(b), a hole-like feature, which possibly caused by vertical motion at the center of the circular fringes, appears at the landward side of the main fringe belt. In Figure 4-2(c), some additional loose fringes appear around the dense fringes, which might be caused by smaller amplitude of tidal vertical motion due to bedrock topography or a temporal variation in ice velocity in the line of sight. Therefore, the GLL delineation required careful examination of available interferograms and possible GZ features. The delineated GLLs for the analyzed time series are shown in Figure 4-3.
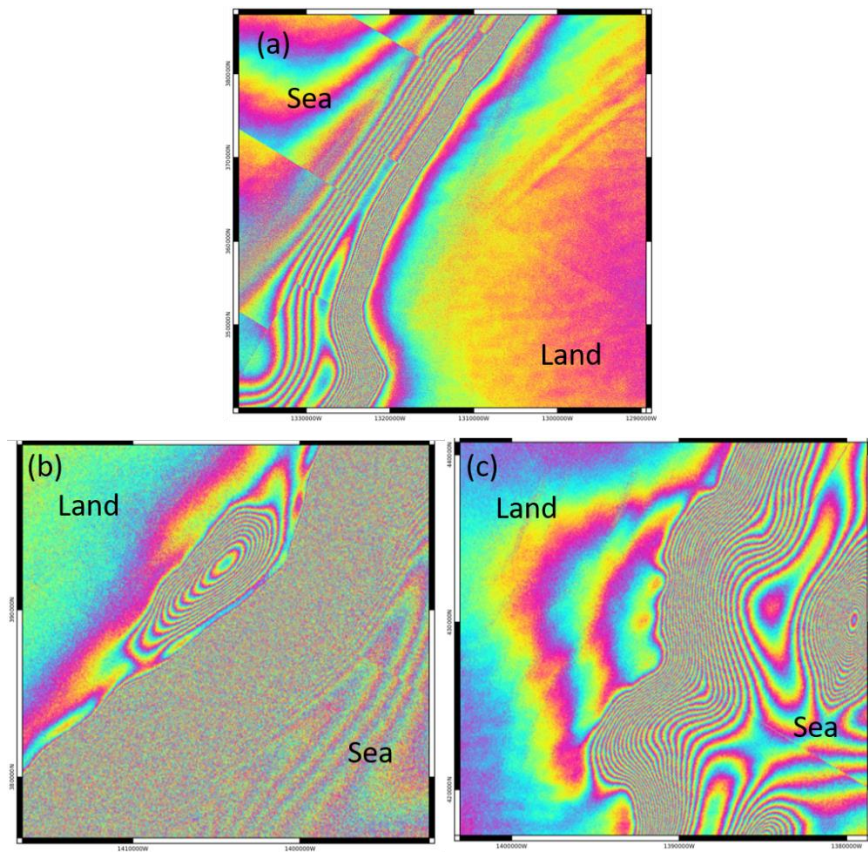
Figure 4-2 GZ on a DInSAR interferogram. (a) Typical GZ feature. (b) Hole-like feature at landside of fringes. (c) Combination of dense fringe with loose fringe.
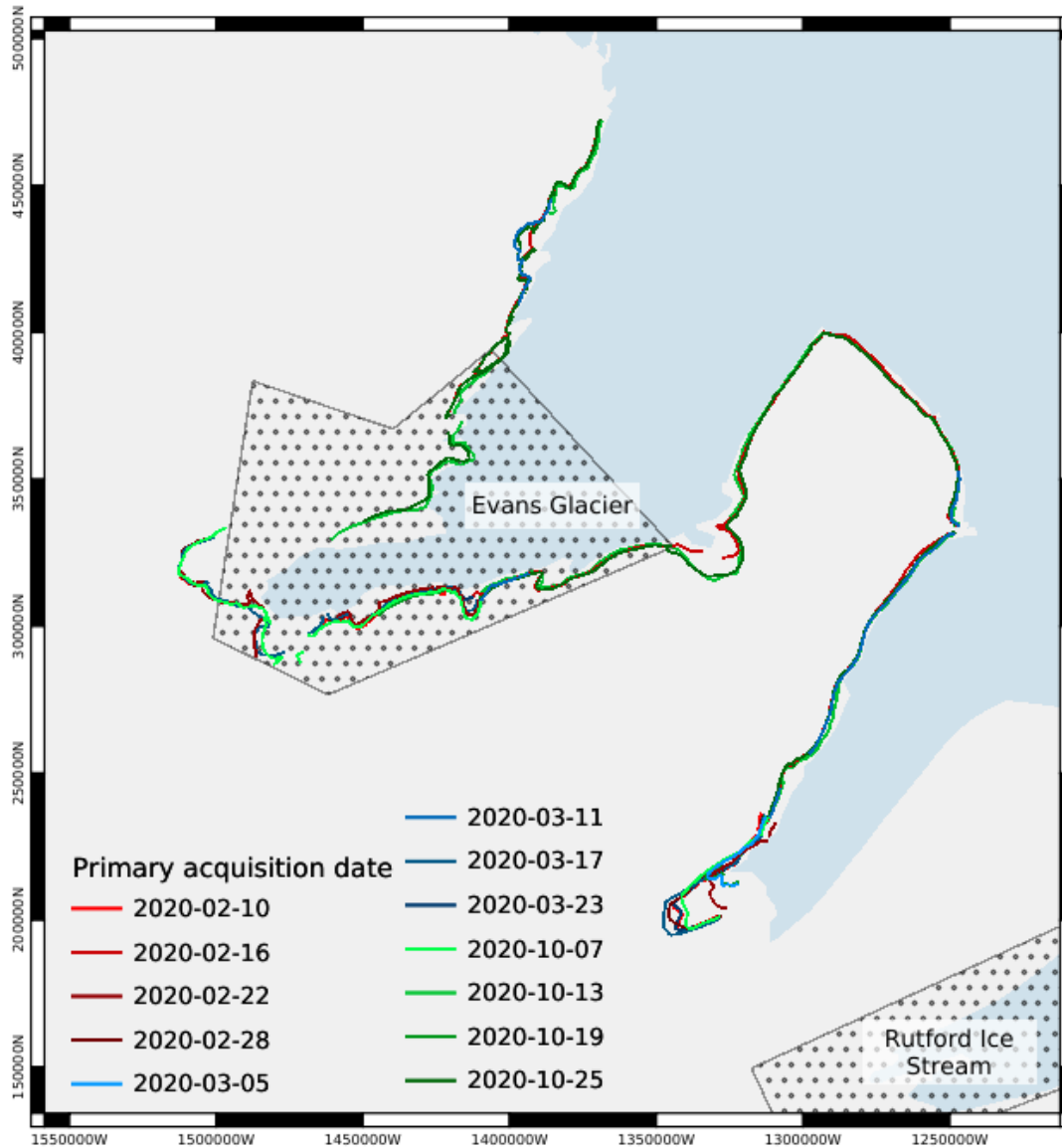
Figure 4-3 Manually delineated GLLs overlaying key glaciers annotation. Color of GLL indicates different acquisition time of scenes.

It is noticed that some locations show significantly larger GLL migration, in particular locations where loose fringes appear (Figure 4-4). Here, the distance between delineated GLLs can reach kilometer magnitude.
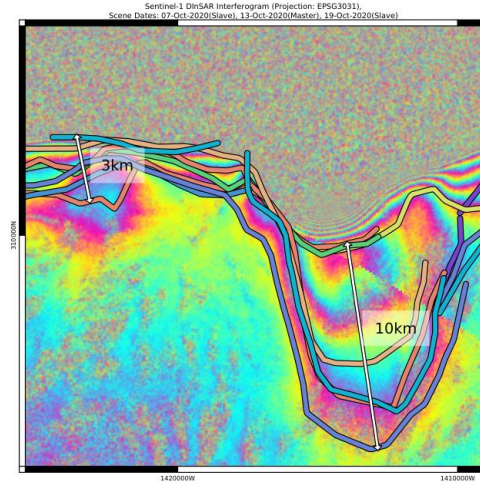
Figure 4-4 Difference in GLL migration extent.

An average GLL was computed with an algorithm outlined in section 3.6.1 Reference GLL generation. Figure 4-5 shows the result generated in each step. From Figure 4-5(a), one can see that the medial axis (black line) of the concave hull polygon (red polygon) is already a 'proxy average' of the GLL dataset. Nevertheless, this proxy is not good enough because the distribution (density) of GLL dataset is not taken into account. One can see, comparing to the medial axis, that the average GLL (Figure 4-5 (d), Red line) approaches to where GLL segments are clustered more densely together.
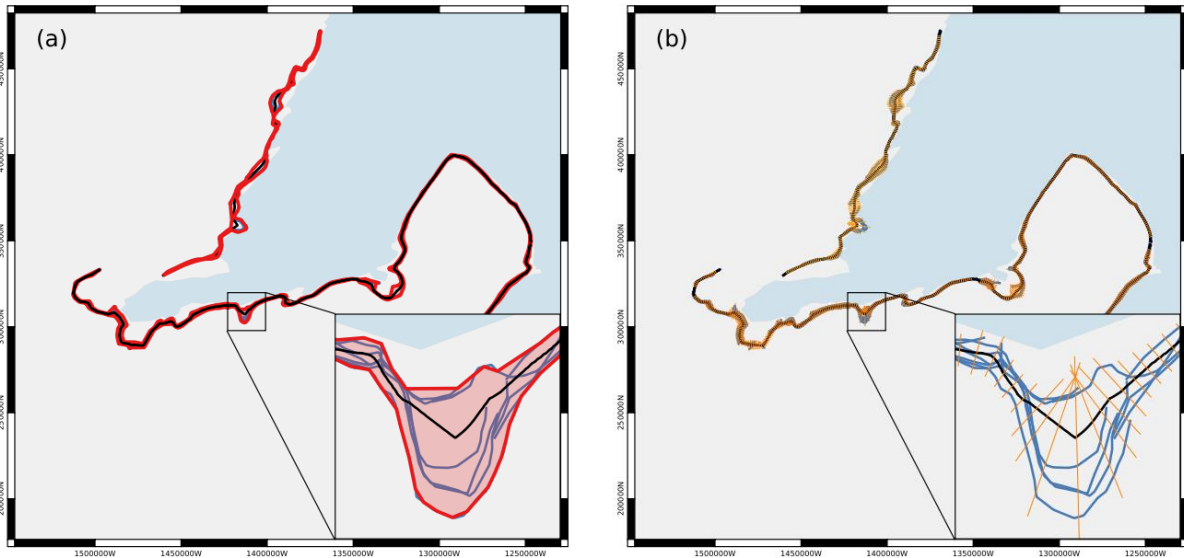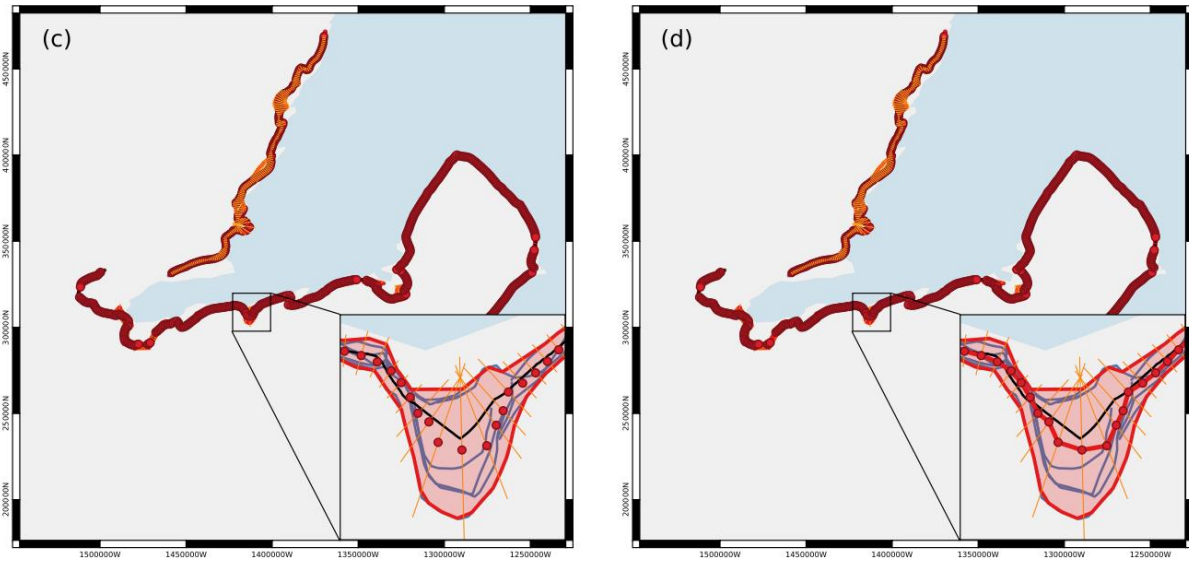
Figure 4-5 Features generated in each step of the GLL average algorithm, with GLL dataset as Blue Line. (a) Concave hull (Translucent red polygon) and medial axis (black line). (b) Normals of medial axis (orange line). (c) Centroids (average points) (red marker) of normal-GLL intersection points. (d) Average GLL (red line).

For better performance, the normal was trimmed according to the concave hull polygon (Figure 4-5(b)). If a normal is too long, it crosses other parts of the GLL segments, leading to a wrong computation of centroids (Figure 4-6(a)). Most of these occurrences have been solved by trimming the normal to appropriate length. However, there is still the chance of multiple intersections between normals and single GLL due to the geometry of the GLL (Figure 4-6(b)), which was corrected by only including the intersection nearest to the medial axis in the average position.
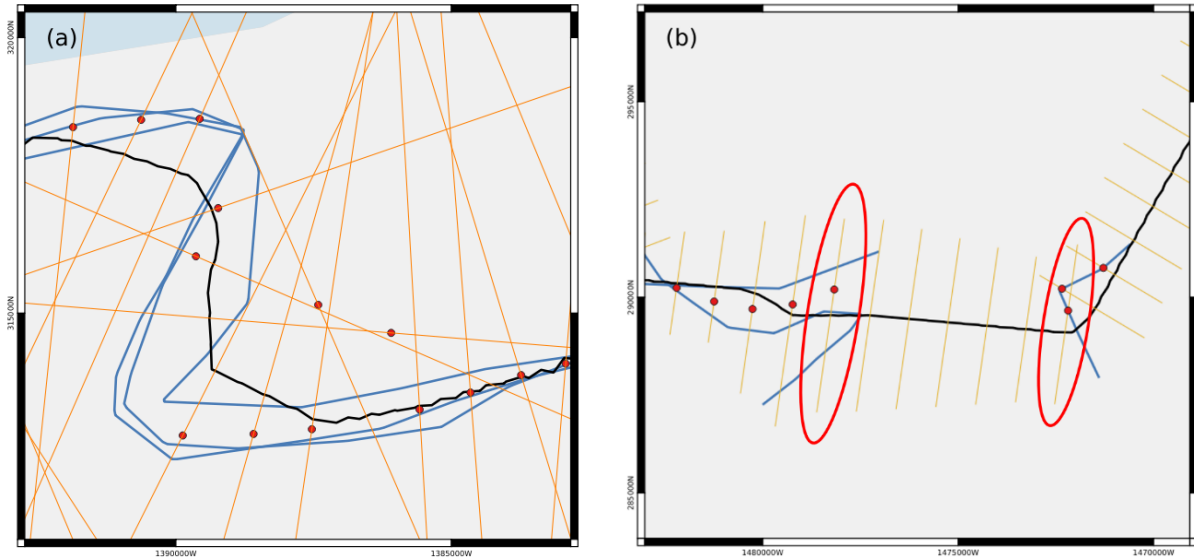
Figure 4-6 Potential problem of multiple intersection between normal and GLL. (a) Wrong centroid computation due to excessive length of the normal. (b)Multiple intersections (Red circles) due to GLL geometry, correction by only counting the nearest intersection.

The performance of the algorithm is satisfactory. Figure 4-7 shows examples of averaging results of GLL segments with complex geometry, often featured with sharp turns or large GLL difference.
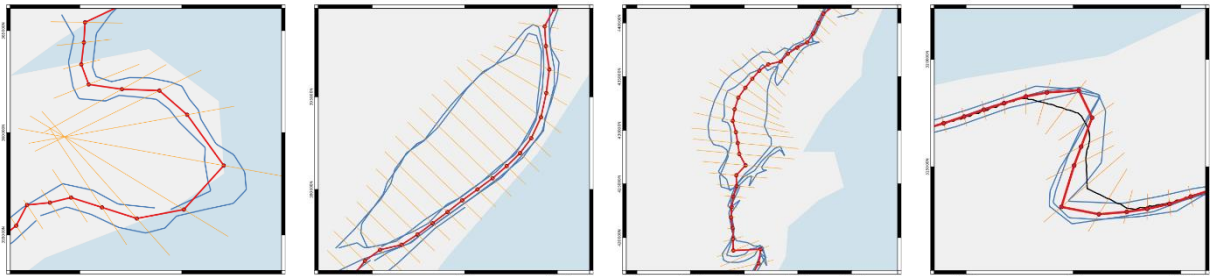
Figure 4-7 Examples of Averaging Result of GLL segments with complex geometry.

The GLL average algorithm is a semi-automatic algorithm, which in theory could also be applied to other line averaging tasks. To better utilize the algorithm, there are manual input parameters that require fine-turning and trial-and-error from users, e.g. dividing groups of GLLs according to a priori knowledge of the geographic location, spacing of normal (Figure 3-8) Δl, distance for computing normal. In particular, changing Δl has a major impact on the performance.

A smaller Δl is a better proxy of the normal line of the tangential surface at the point where the normal should be calculated. Yet, a larger Δl produces a more stable averaging result, since it is less influenced by small fluctuations in the medial axis, and more likely to capture the maximum extent of GLL datasets (Figure 4-8).
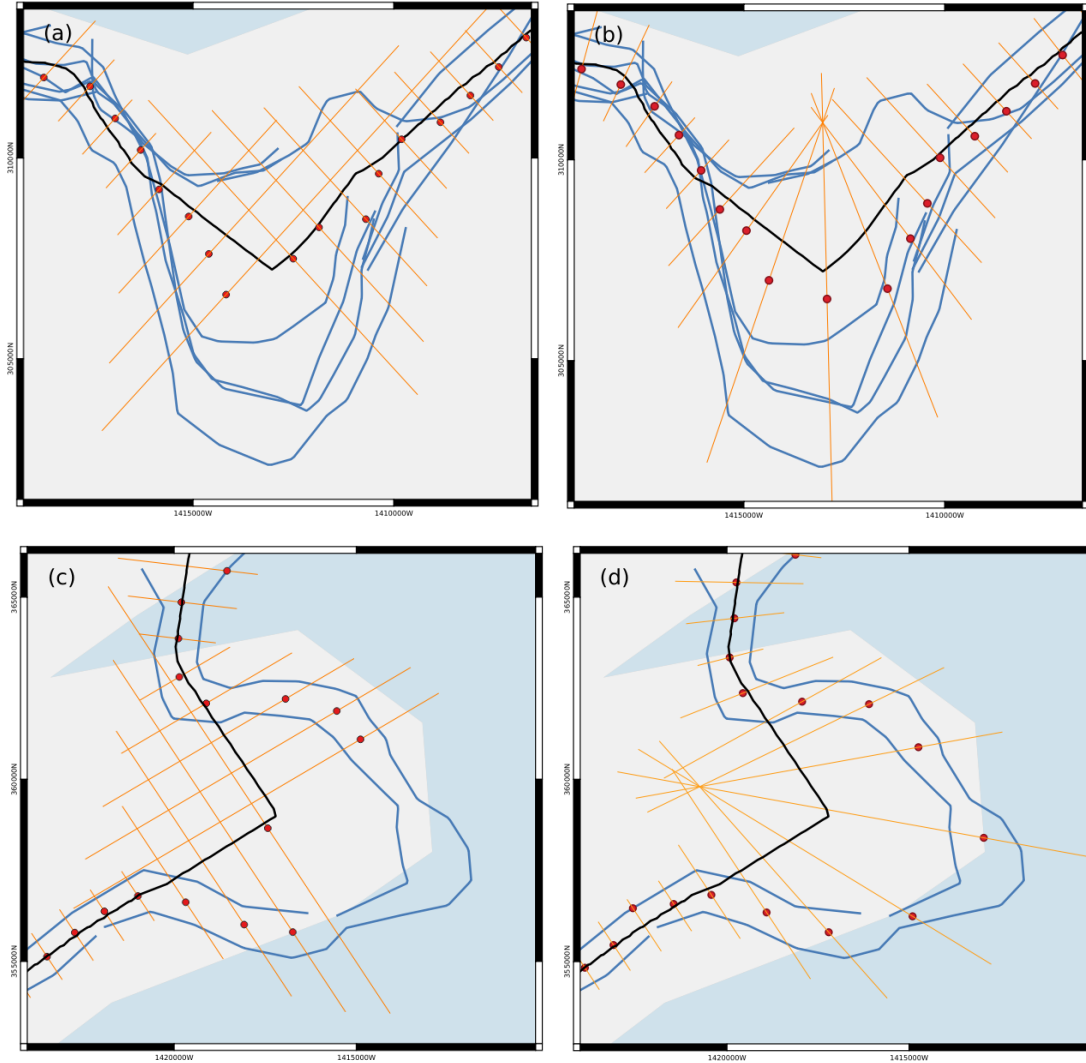
Figure 4-8 Comparison of averaging performance.

(a) Example 1, $\Delta l = 100m$. (b) Example 1, $\Delta l = 5000m$.

(c) Example 2, $\Delta l = 100m$. (d) Example 2, $\Delta l = 5000m$.

After computing the average GLL, the GLL migration was computed as described in section 3.6.2 GLL migration. The GLLs were converted to a point cloud with 1km sampling along the lines (Figure 4-9(a)), serving as neighbor GLL for the point-line method. The bounding boxes (Figure

4-9(b)) for the box method were manually drawn in order to fit the orientation of GLL and the extent of GLL migration.
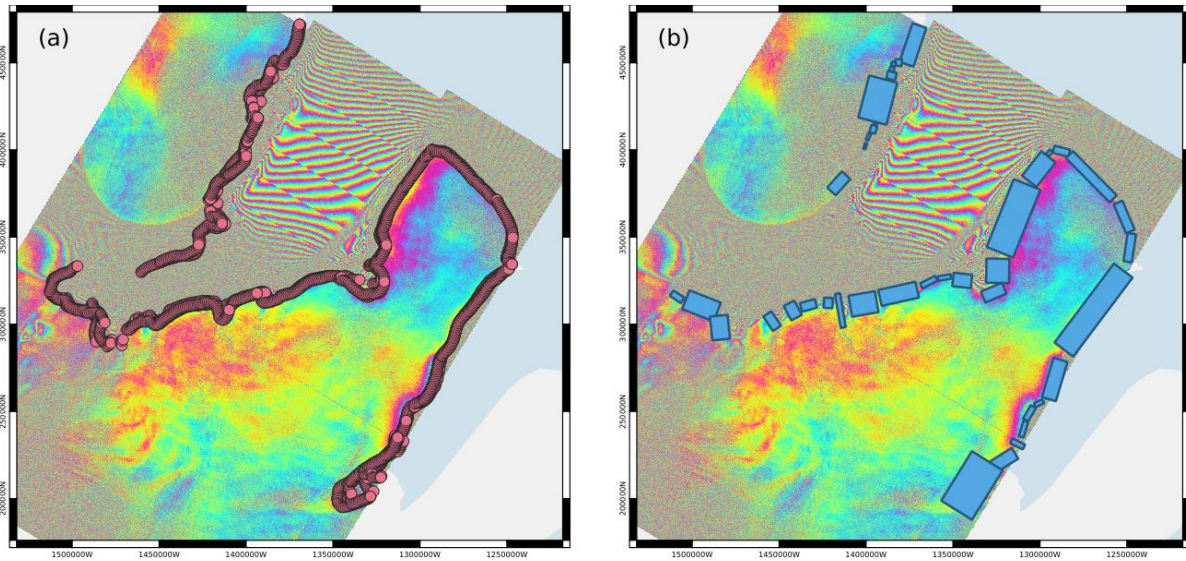
Figure 4-9 (a) GLL Point Cloud with 1km spacing. (b) Bounding Boxes.

The result of GLL migration are as follow (Description of Parameters in Table 3-3):

Table 4-2 GLL Migration Results in meters.

	Mean Migration	Maximum Migration	Migration from Average
Point-Line Method	1270.10	1333.02	761.12
Box Method	1163.83	1361.17	753.92
Intersection Method	1554.85	1519.71	732.61

The results shown in Table 4-2 indicate that short-term fluctuations of the GLL, regardless of causes and method, is at the scale of kilometers. The results computed by the point-line method and box method are similar, with a difference of around 100m, which suggests that both methods reach similar level of robustness in term of quantifying GLL migration. The results computed by the intersection method slightly deviate from the other two.

For comparison, the long-term GLL migration against GLL delineated from ERS scenes acquired during 1994-1996 in AIS_cci GLL dataset was computed (Figure 4-10, Table 4-3).

41

Table 4-3 Long-term GLL Migration Results in meters.

	Mean Migration
Intersection Method	2540.28
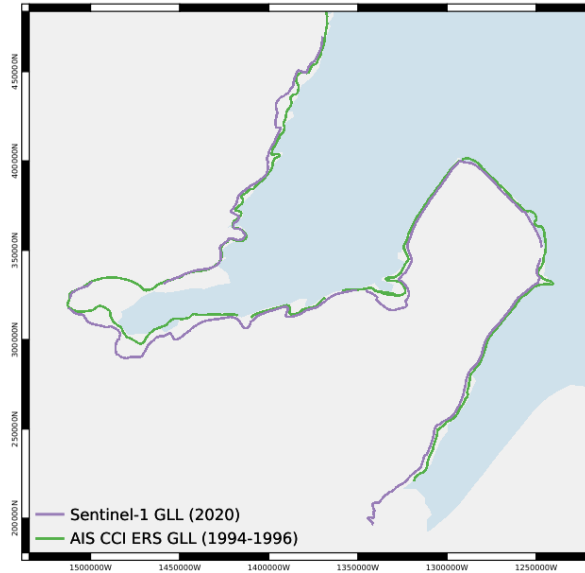
Figure 4-10 GLL migration against ERS GLL.

The results in Table 4-2 and Table 4-3 show that short-term fluctuations of GLL are on a similar level than long-term migration. In some sections along the grounding line, however, a melting induced long term retreat could be detected. Since GLL has significant short-term fluctuation signal, an average GLL for a GLL dataset is necessary to be computed, serving as a more robust representation for GLL at certain period when quantifying GLL retreat due to climate change.

4.2 Bedrock slope and Ocean Tides: Special Features and Characteristics

In this section, the variation of bedrock elevation and tides at the test region is discussed.
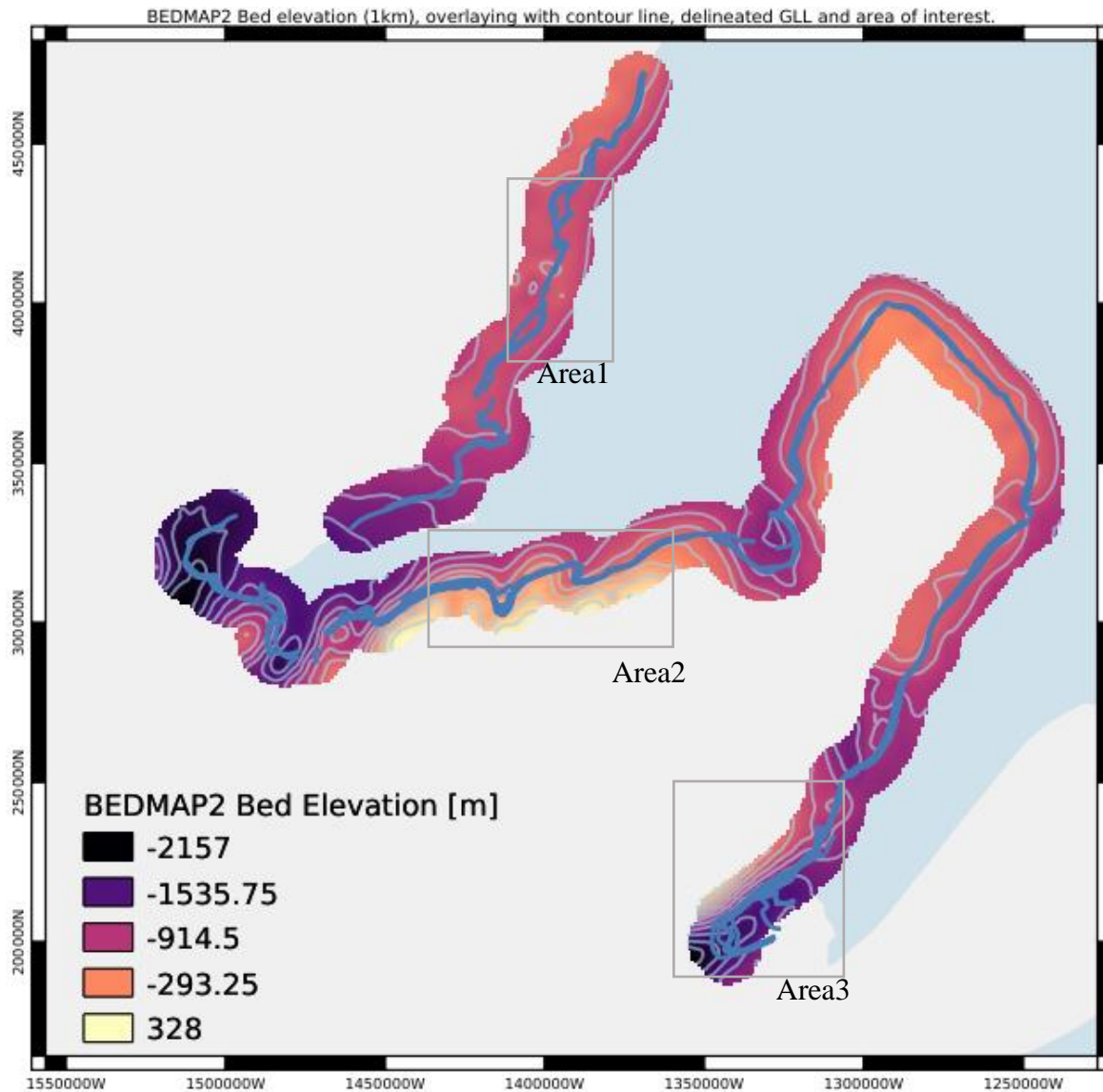
Figure 4-11 BEDMAP2 Bedrock elevation. The layer is clipped to enhance contrast of data at the region of interest.

Figure 4-11 displays the bed elevation, clipped to the region of interest. In the test region, most of the GLL segments are laying on a prograde slope (Area 2), or a relatively flat surface (Area 1). In general, one can see that the shape of the GLL followed the shape of the contour lines. Both in Area 1 and Area 2, small 'bubbles' of significant GLL migration could be found, yet the two bed elevation profiles are quite different. Retrograde slopes could be found in Area 3 where significant GLL migration was also detected.

With localized migration computed from equation (3.3), Figure 4-12 shows the comparison between average GLL migration and bedrock slope in different locations. Significant GLL migration was more favorable at location with gentle bed slope, which might indicate that steep slope is not favorable for GLL migration.
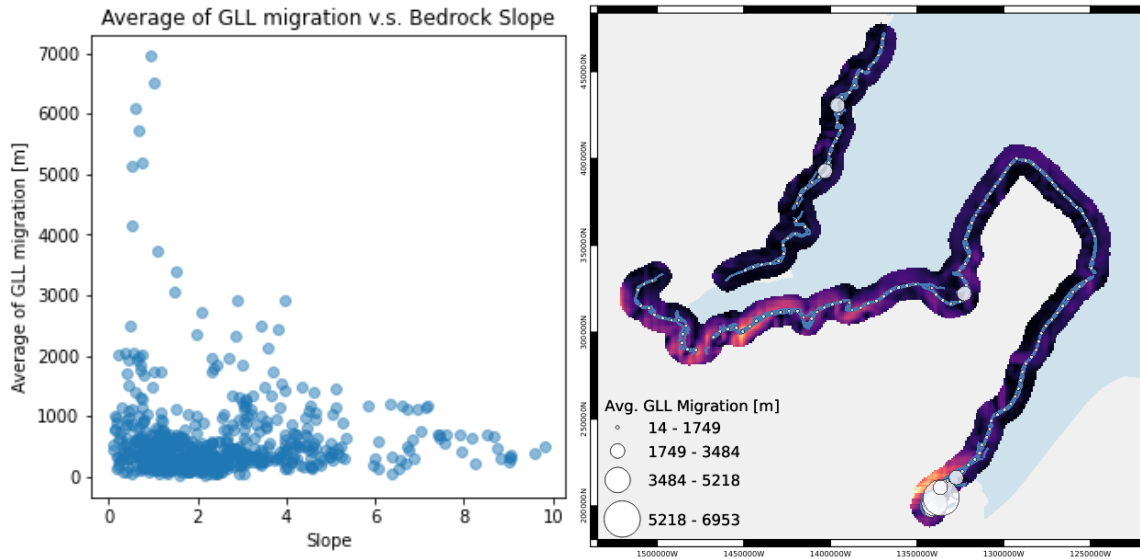
Figure 4-12 Avg. GLL Migration v.s. Bedrock Slope. (Left) Scatter Plot. (Right) Map View.
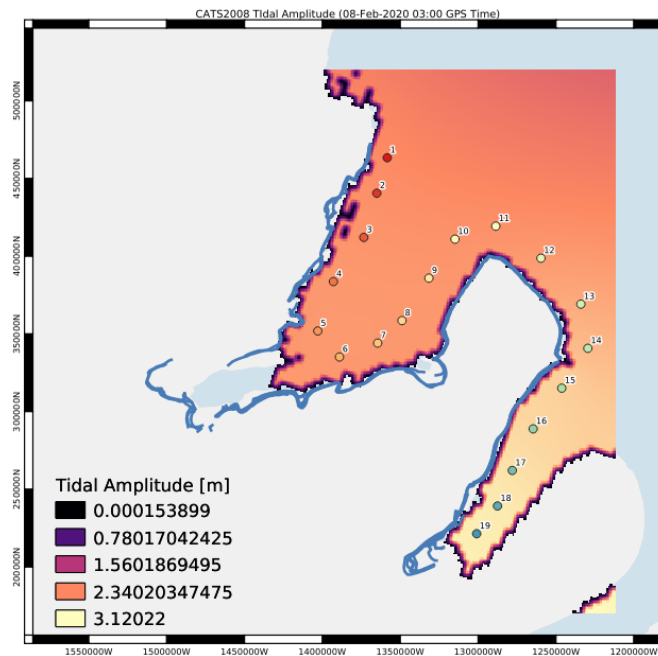
Figure 4-13. CATS2008 Ocean Tidal Amplitude on 08-Feb-2020 03:00 GPS Time. Dots are customized tidal points for validation.

To investigate the variation of ocean tidal amplitude at test region, the tidal amplitude on 08-Feb-2020 03:00 GPS Time (Figure 4-13) was generated from the CATS2008 tide model (section 2.3 Ocean Tides). This time is chosen because there is a high tide, thus amplifying the difference in ocean tide level in the bay.

From Figure 4-13, one can see that the InSAR derived GLL is located more landward than the boundary of the model domain of the CATS2008 model. Therefore, tidal height could not be predicted directly at the GLL. In order to annotate the GLL segments with tide information, customized points for tide analysis were picked at a distance of approximate 10 km to the boundary of the model domain.

To further investigate the temporal variation of ocean tides in different locations, tidal time series corrected by air pressure were generated at 19 customized points (Figure 4-14).
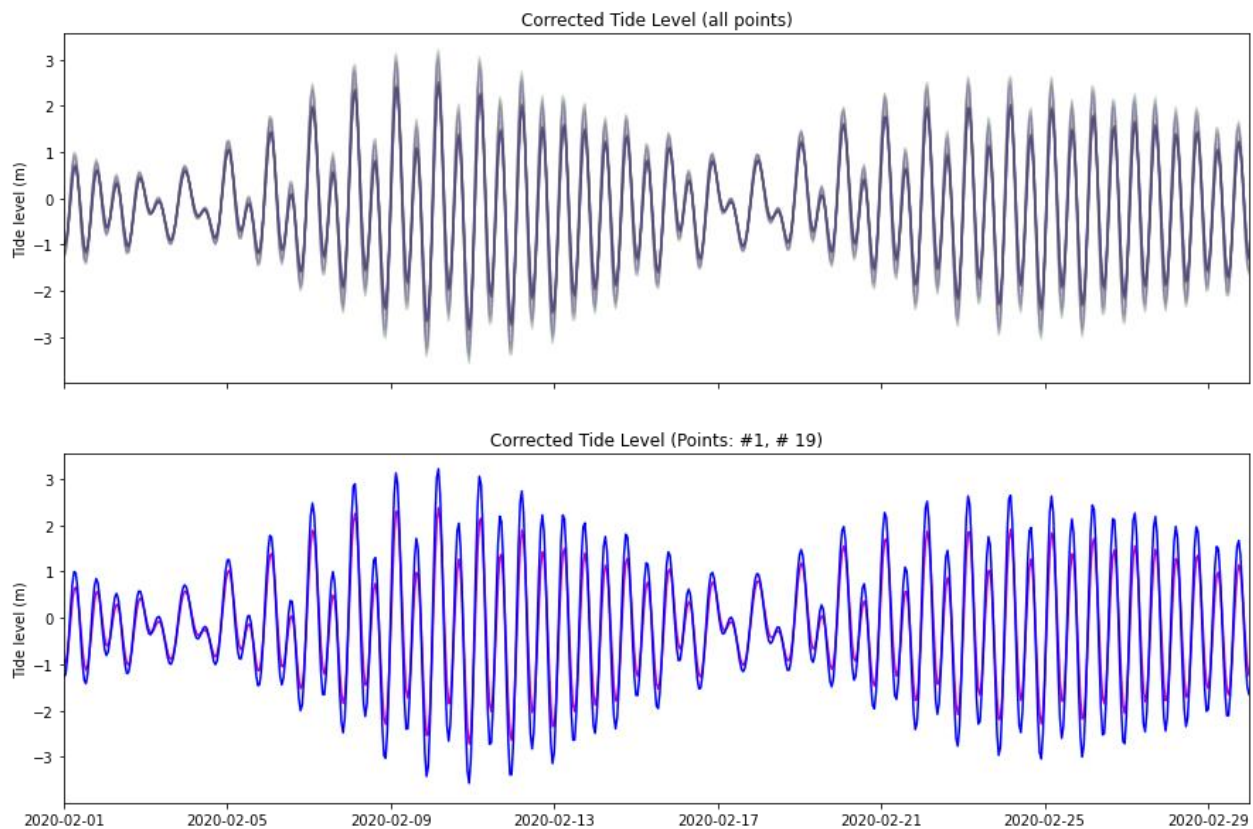
Figure 4-14 Ocean Tidal Time Series. (Above) All Points. (Bottom) Example of comparison between Point #1 and #19.

It is found that ocean tidal signals in the test region, which is less than 400 km wide, appeared to be constructed by the same signal components, always synchronized, and thus only differ in magnitude. Therefore, a time-series analysis with respect any single point in the bay is representative for testing correlation of oceanic tide and GLL migration.

Since the variation of ocean tidal magnitude at open water was much smaller than the converging model boundary, a relatively seaward point was chosen, even though it is further away from the GLL, for tidal computation in the time series analysis of the next section.

4.3 Time Series Analysis

Time Series Analysis was carried out in 3 different averaging scales (Figure 4-15). For the smallest scale, the time series averaged only GLL migration in specified key areas, which feature significant GLL migration. Then, average for major GLL line segments, which are separated geographically, were computed. Lastly, an average was computed for the whole region.
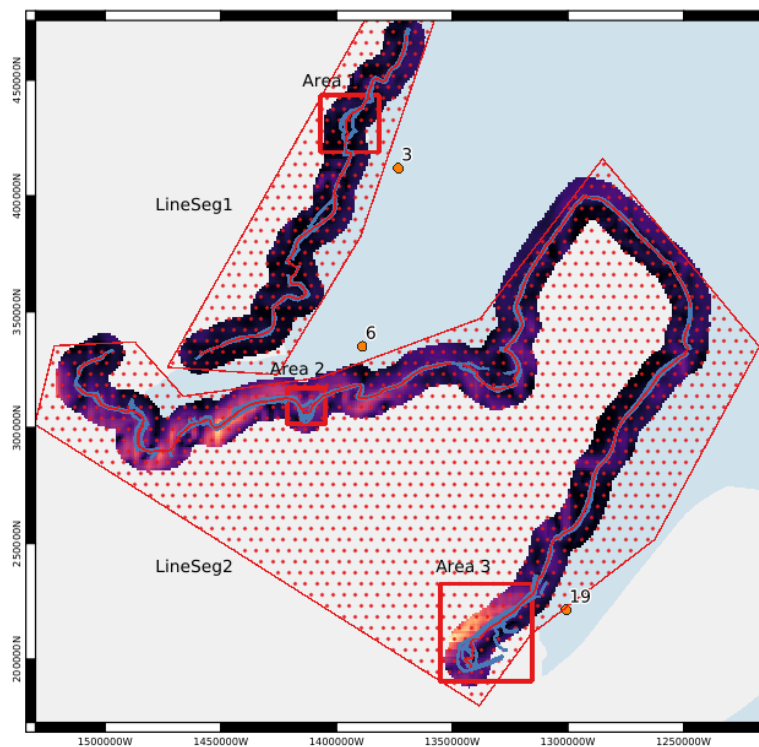
Figure 4-15 Time Series Parameters. Averaging areas overlaying on Slope map derived from BEDMAP2 Bed Elevation.

Regarding the tidal points, the 3 points indicated in Figure 4-15, which are corresponding to Point #3,6,19 in Figure 4-13, were used for generating ocean tides time series. Since it has been shown in previous section that ocean tide level does not vary significantly spatially, the mean value of the tidal time series of these 3 points was used for comparison for GLL migration of major line segments and the whole region.

The bedrock slopes (displayed in Figure 4-15) of the 3 areas were as follow:

Table 4-4 Bedrock Slope of key areas.

Area 1	0.51
Area 2	5.43
Area 3	1.07

Results are shown in Figure 4-16, Figure 4-17, Table 4-5 and Table 4-6.

Figure 4-16 Interferograms' Timeseries.

Table 4-5 Corrected Ocean Tides of each DInSAR combination and No. of fringes. Description of rows in Table 3-3.

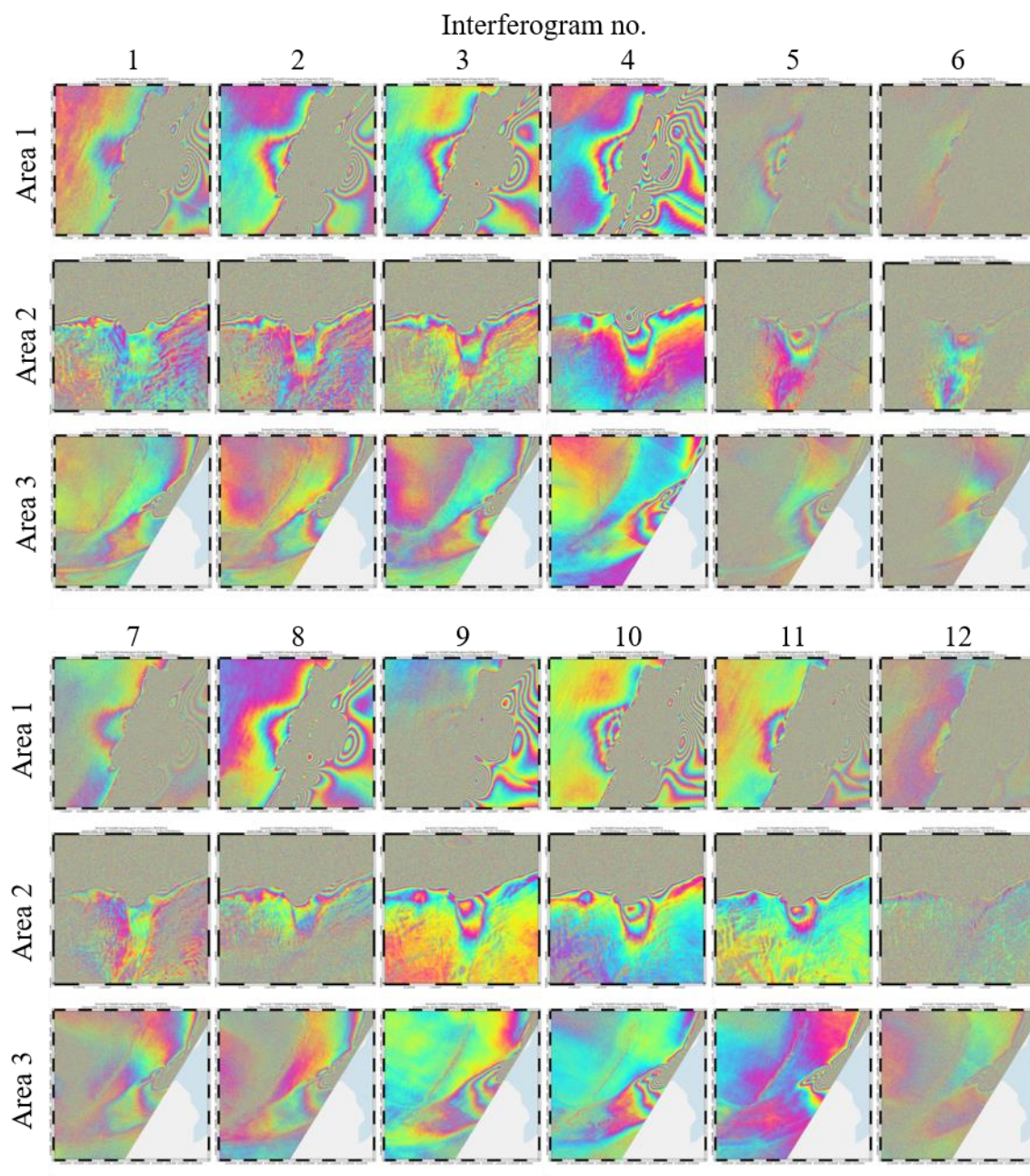| Interferogram no.	1	2	3	4	5	6	7	8	9	10	11	12
T1 (Secondary)	04-Feb-2020	10-Feb-2020	16-Feb-2020	22-Feb-2020	28-Feb-2020	05-Mar-2020	11-Mar-2020	17-Mar-2020	01-Oct-2020	07-Oct-2020	13-Oct-2020	19-Oct-2020
T2 (Primary)	10-Feb-2020	16-Feb-2020	22-Feb-2020	28-Feb-2020	05-Mar-2020	11-Mar-2020	17-Mar-2020	23-Mar-2020	07-Oct-2020	13-Oct-2020	19-Oct-2020	25-Oct-2020
T3 (Secondary)	16-Feb-2020	22-Feb-2020	28-Feb-2020	05-Mar-2020	11-Mar-2020	17-Mar-2020	23-Mar-2020	29-Mar-2020	13-Oct-2020	19-Oct-2020	25-Oct-2020	31-Oct-2020
Mean COR_OTL_T1	-0.13	2.70	-0.29	1.85	1.20	0.13	2.34	-0.21	1.46	1.43	-0.72	2.84
Mean COR_OTL_T2	2.70	-0.29	1.85	1.20	0.13	2.34	-0.21	1. 65	1.43	-0.72	2.84	-0.62
Mean COR_OTL_T3	-0.29	1.85	1.20	0.13	2.34	-0.21	1.65	0.83	-0.72	2.84	-0.62	1.62
Mean DH1	2.83	-2.99	2.14	-0.65	-1.07	2.21	-2.55	1.86	-0.03	-2.15	3.56	-3.46
Mean DH2	2.99	-2.14	0.65	1.07	-2.21	2.55	-1.86	0.82	2.15	-3.56	3.46	-2.24
Mean DHF	5.82	-5.13	2.79	0.42	-3.28	4.76	-4.41	2.68	2.12	-5.71	7.02	-5.7

Table 4-6 GLL Migrations of each DInSAR combination. Landward migrations are with positive sign.

| Interferogram no./ Statistics	1	2	3	4	5	6	7	8	9	10	11	12	Min	Max	Mean
Area 1	N/A	-669.17	N/A	N/A	742.97	N/A	N/A	N/A	-1609.42	N/A	262.46	N/A	-1609.42	742.97	-318.29
Area 2	-971.02	-649.31	311.37	485.38	283.56	N/A	-691.89	-31.19	-435.62	1344.99	440.76	565.80	-971.02	1344.99	59.35
Area 3	N/A	69.98	296.79	-1737.74	N/A	733.53	-150.24	586.61	N/A	970.30	N/A	550.09	-1737.74	970.30	164.92
LineSeg1	46.01	N/A	N/A	N/A	497.59	N/A	N/A	N/A	-554.54	N/A	251.40	N/A	-554.54	497.59	60.11
LineSeg2	34.75	236.84	146.75	-673.02	-92.70	690.62	-223.47	70.67	-341.53	352.11	288.03	677.83	-673.02	690.62	97.24
Whole Region	37.74	236.84	146.75	-673.02	44.81	690.62	-223.47	70.67	-393.02	352.11	276.16	677.83	-673.02	690.62	103.67
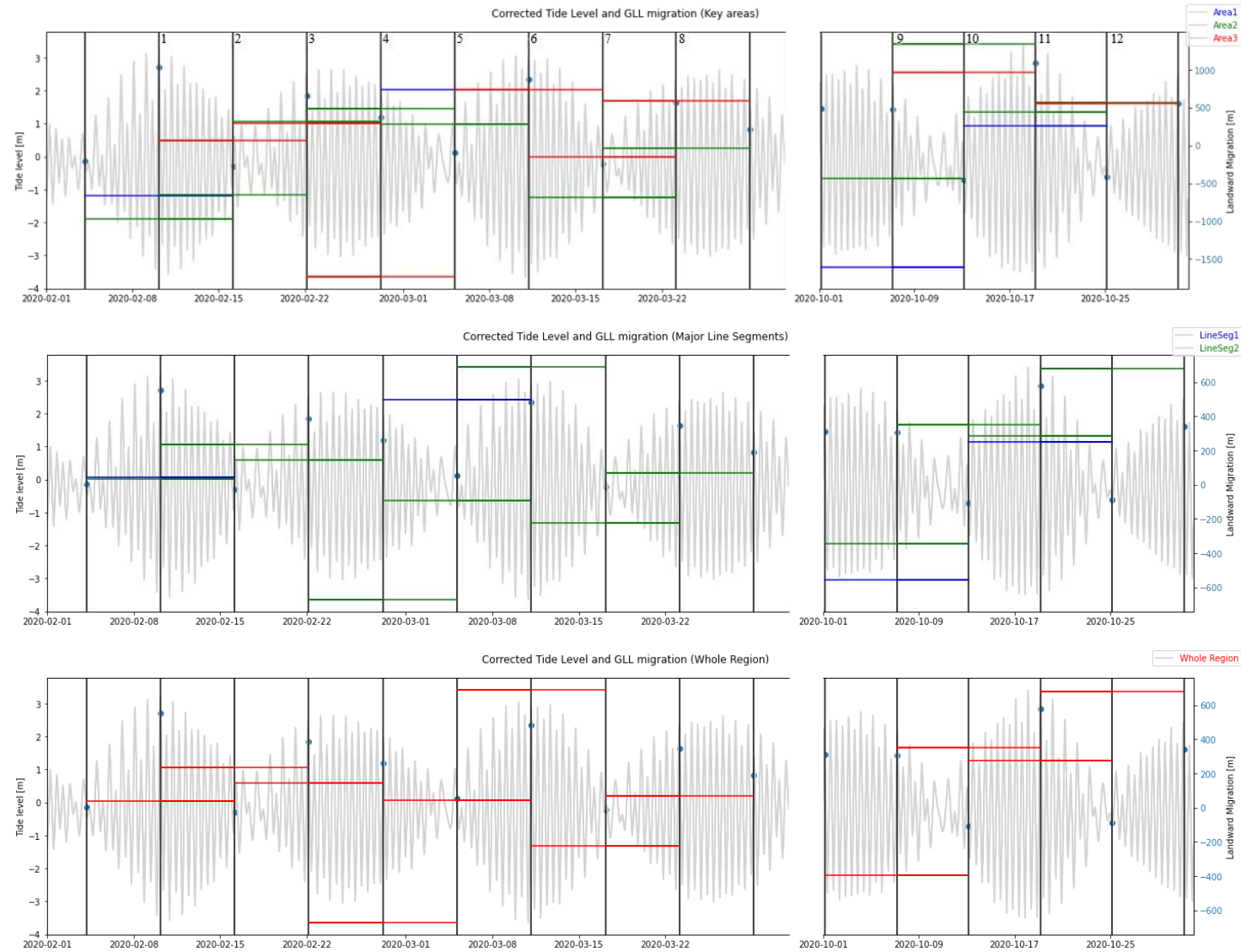
Figure 4-17. Time Series of Corrected Ocean Tide Level and GLL migration. (Top) Key areas, dates of primary scenes are annotated with corresponding interferogram no. in Table 4-5. (Middle) Major Line Segments. (Bottom) Whole Region.

Counting fringes was a difficult task because GZ often decorrelated when the fringes were too densely packed, thus only qualitative description is given here. In general, the fringe density variations in the 3 areas behaved similar as they are under the effect of a similar tidal cycle. It is observed that, the GZ appears as less dense fringes when the magnitude of double difference of tidal difference DHF was small. This can be observed in interferogram no. 4. The effect is expected because the DHF measurement directly specifies the modelled vertical displacement that should be measured in the DInSAR interferogram. There existed tide combinations where vertical tide displacements cancel out when combining the three S1 acquisitions into a triplet. The contrary effect can be seen for example in interferogram no.1 or no.2 where DH1 and DH2 have the same sign and their vertical displacements are added when forming the triplet in this way.

These areas also could be divided in terms of GLL migration (Table 4-5). In interferograms no. 1-3, a landward migration could be found; while in Interferogram no. 9-11, a seaward migration of GLL could be found in these areas.

However, to interpret the relationship between GLL migration and ocean tides is difficult. There is no distinct difference in ocean tide levels, or tidal double difference, between the 2 set of interferograms (1-3, 9-11). The correlation between GLL migration and ocean tides does not improve after considering averaging scales (Figure 4-16).

4.4 Discussion

In terms of finding out how ocean tides contribute to short-term GLL migration, the results indicate that there might be still room of improvement in methodology or limitations of current data and technology.

First, the temporal resolution of a repeat-pass InSAR is limited. Figure 4-17 has shown that the acquisition period of the DInSAR interferogram is across almost half of an ocean tide cycle, while ocean tides are changing in hours. It is questionable, whether the response of GLL migration to ocean tides changes could be well observed. In particular, it is suspected that there might existing lagging between ocean tides changes and ice shelf response.

In addition, as mentioned in section 2.2.2 SAR Interferometry (InSAR), repeat-pass InSAR is vulnerable to temporal decorrelation. In the context of observing tidal deflection of ice

51

shelf, it is possible that there are changes in ice velocity in LOS, e.g. horizontal component of ocean tide induced velocity. In other words, assumption for equation (2.5) is violated since horizontal ice motion is not constant which can contribute to the LOS component depending on its horizontal flow direction relative to the satellite's flight path. These changes might cause additional fringes on the interferogram, which might be interpreted as an uplift due to ocean tides, thus leading to a wrongly delineated GLL.

To put it in another way, more information is needed to differentiate the contribution of horizontal and vertical ice motion to the LOS displacement which is observed in this study. (Rignot, 1998) used a model-fitting technique based on an elastic-beam theory to detect the landward limit of the GZ (point **F**). This possibly helps separating the two motion components, which is not always possible by visual inspection. In the elastic beam model, only vertical motion that is characteristic to ice shelf bending would be used to obtain the point of ungrounding. Therefore, the accuracy of GLL delineation should improve with the aid of a numerical model like the elastic-beam model. It can even lead to the development of a robust automatic delineation algorithm.

There is also possibility that no correlation could be found because of erroneous model output for the oceanic tides, yet this scenario is unlikely because DHF shows correlation with the number of fringes by inspection. In addition, previous studies have shown that oceanic tides from the CATS2008 model and measured interferometric displacements agree (Wild et al., 2018).

CHAPTER 5
Conclusion and Outlook

5.1 Summary and Conclusion

The migration of the glacier grounding line, the boundary between grounded ice and floating ice, is an important indicator of ice sheet stability in a warming climate. Ice-shelf thinning induces grounding line retreat, and potentially leads to the collapse of the inland catchment areas centennial time frames. Therefore, a continuous observation of the grounding line position is of interest for ice sheet modelling and also to predict future sea level rise. However, grounding line in nature is not static in position and it is subject to short-term fluctuations which are influenced by changes in ocean tide level and atmospheric pressure. Investigating tidal influence to the grounding line helps separating the tidal signal from the long-term migration because of ice shelf thinning. Also, it helps quantifying ice discharge and ice flow, as well as potential melting underneath the ice, due to intrusion of sea water.

In this study, the correlation between the time series of grounding line, derived from Sentinel-1 DInSAR interferograms and the ocean tide level computed from CATS2008 tide model and air pressure corrected with NCEP reanalysis data were investigated.

This study has quantified the short-term variations in GLL position and developed a robust GLL averaging algorithm. It has been shown that short-term GLL migration can be on the kilometer scale, thus GLL averaging will be helpful in terms of serving as a more robust representation for GLL at certain period when quantifying long-term GLL retreat due to climate change. Although significant short-term migration was observed, this study was not able to find a correlation between ocean tide levels and the GLL position which explains the cause of such short-term migration.

5.2 Outlook

This section is dedicated to suggest future possible studies, in order to tackle limitations discussed in section 4.4 Discussion, in particularly to explain the cause of short-term migration of GLL.

It is suggested to repeat the experiment again when scenes with shorter repeat cycle are available, alleviating the problem of temporal correlation. This could be the case in future SAR missions or if the Sentinel-1 constellation is placed in a configuration with short repeat cycles of less than 6 days.

Although sea surface temperature is a key parameter, data is not available at the test region because it is too far inland (about 550 km from the coast) and the ocean is covered by sea ice. The problem of the over-extended land mask is also occurred at ocean tides prediction. To better quantify melting occurring under ice shelves, modelling ocean temperature for region covered by sea ice will be of use.

Entering the era of artificial intelligence, (Mohajerani et al., 2021) have attempted to delineate GLL automatic using deep learning recently. Though the automatic delineated GLL still significantly deviated from existing manual delineated GLL products, it is well-noted that integration with artificial intelligence technology is the major trend of future development. Nevertheless, it is still worthwhile to assimilate numerical model like the elastic beam model, which contains information on the physical processes, to the delineation procedure. This could separate horizontal displacements from tide-induced velocity changes and vertical displacements caused by tidal bending of the ice shelf. With the help of this model the accuracy of manual delineation can be improved in the short-term or the delineation process could be replaced with a robust automatic algorithm in the long-term.

REFERENCES

Bamler, R. (2000). Principles Of Synthetic Aperture Radar. *Surveys in Geophysics*, *21*. https://doi.org/10.1023/A:1006790026612

Bamler, R., Eineder, M., Kampes, B., Runge, H., & Adam, N. (2003). SRTM and beyond: Current situation and new developments in spaceborne InSAR. *Proceedings of the ISPRS Workshop on High Resolution Mapping from Space*, 6–8.

Bindschadler, R., Choi, H., Wichlacz, A., Bingham, R., Bohlander, J., Brunt, K., Corr, H., Drews, R., Fricker, H., Hall, M., Hindmarsh, R., Kohler, J., Padman, L., Rack, W., Rotschky, G., Urbini, S., Vornberger, P., & Young, N. (2011). Getting around Antarctica: New high-resolution mappings of the grounded and freely-floating boundaries of the Antarctic ice sheet created for the International Polar Year. *The Cryosphere*, *5*(3), 569–588. https://doi.org/10.5194/tc-5-569-2011

British Antarctic Survey. (2005, May). Antarctic Factsheet. *British Antarctic Survey*. https://www.bas.ac.uk/science/science-and-society/education/antarctic-factsheet-geographical-statistics/

Brunt, K. M., Fricker, H. A., Padman, L., Scambos, T. A., & O'Neel, S. (2010). Mapping the grounding zone of the Ross Ice Shelf, Antarctica, using ICESat laser altimetry. *Annals of Glaciology*, *51*(55), 71–79. https://doi.org/10.3189/172756410791392790

Bryan, F. (1986). High-latitude salinity effects and interhemispheric thermohaline circulations. *Nature*, *323*(6086), 301–304.

Bürgmann, R., Rosen, P. A., & Fielding, E. J. (2000). Synthetic Aperture Radar Interferometry to Measure Earth's Surface Topography and Its Deformation. *Annual Review of Earth and Planetary Sciences*, *28*(1), 169–209. https://doi.org/10.1146/annurev.earth.28.1.169

Chowdhury, T., Floricioiu, D., Baessler, M., & Parizzi, A. (2016, October 13). *Automatic grounding line derivation over Antarctic Ice Sheet from ERS-1/2, Sentinel-1 and TerraSAR-X*.

Cook, A. J., & Vaughan, D. G. (2010). Overview of areal changes of the ice shelves on the Antarctic Peninsula over the past 50 years. *The Cryosphere*, *4*(1), 77–98.

Cuffey, K. M., & Paterson, W. S. B. (2010). *The Physics of Glaciers*. Academic Press.

Dawson, G. J., & Bamber, J. L. (2020). Measuring the location and width of the Antarctic grounding zone using CryoSat-2. *The Cryosphere*, *14*(6), 2071–2086. https://doi.org/10.5194/tc-14-2071-2020

DLR. (n.d.). *EOC Geoservice Data Guide*. Retrieved June 11, 2021, from https://geoservice.dlr.de/web/dataguide/tdm90/

DLR. (2018). *Grounding line for Actarctica, derived from ERS-1/2 and Copernicus Sentinel-1 data acquired in 1994 -1996 and 2015—2017, Antarctic Ice Sheet CCI, release date 2018-07-02, v1.0.*

Egbert, G. D., & Erofeeva, S. Y. (2002). Efficient Inverse Modeling of Barotropic Ocean Tides. *Journal of Atmospheric and Oceanic Technology*, *19*(2), 183–204. https://doi.org/10.1175/1520-0426(2002)019<0183:EIMOBO>2.0.CO;2

ESA. (2013). *Sentinel-1 User Handbook*.

Floricioiu, D. (2016). *The grounding zone of Darwin Glacier (79°50' S, 159°50' E)*.

Fofonoff, N. P., & Millard Jr, R. C. (1983). *Algorithms for the computation of fundamental properties of seawater.*

Fretwell, P., Pritchard, H. D., Vaughan, D. G., Bamber, J. L., Barrand, N. E., Bell, R., Bianchi, C., Bingham, R. G., Blankenship, D. D., Casassa, G., Catania, G., Callens, D., Conway, H., Cook, A. J., Corr, H. F. J., Damaske, D., Damm, V., Ferraccioli, F., Forsberg, R., … Zirizzotti, A. (2013). Bedmap2: Improved ice bed, surface and thickness datasets for Antarctica. *The Cryosphere*, *7*(1), 375–393. https://doi.org/10.5194/tc-7-375-2013

Fricker, H. A., Coleman, R., Padman, L., Scambos, T. A., Bohlander, J., & Brunt, K. M. (2009). Mapping the grounding zone of the Amery Ice Shelf, East Antarctica using InSAR, MODIS and ICESat. *Antarctic Science*, *21*(5), 515–532. https://doi.org/10.1017/S095410200999023X

Gleick, P. H. (1993). Water in crisis. Pacific Institute for Studies in Dev. *Environment & Security. Stockholm Env. Institute, Oxford Univ. Press*, *473*, 9.

Gonzalez, F. R., Adam, N., Parizzi, A., & Brcic, R. (2013). The Integrated Wide Area Processor (IWAP): A processor for wide area persistent scatterer interferometry. *ESA Living Planet Symposium*, *722*, 353.

Kalnay, E., Kanamitsu, M., Kistler, R., Collins, W., Deaven, D., Gandin, L., Iredell, M., Saha, S., White, G., Woollen, J., Zhu, Y., Chelliah, M., Ebisuzaki, W., Higgins, W., Janowiak, J., Mo, K. C., Ropelewski, C., Wang, J., Leetmaa, A., … Joseph, D. (1996). The NCEP/NCAR 40-Year Reanalysis Project. *Bulletin of the American Meteorological Society*, *77*(3), 437–472. https://doi.org/10.1175/1520-0477(1996)077<0437:TNYRP>2.0.CO;2

Krieger, G., Moreira, A., Fiedler, H., Hajnsek, I., Werner, M., Younis, M., & Zink, M. (2007). TanDEM-X: A satellite formation for high-resolution SAR interferometry. *IEEE Transactions on Geoscience and Remote Sensing*, *45*(11), 3317–3341.

Mohajerani, Y., Jeong, S., Scheuchl, B., Velicogna, I., Rignot, E., & Milillo, P. (2021). Automatic delineation of glacier grounding lines in differential interferometric synthetic-aperture radar data using deep learning. *Scientific Reports*, *11*(1), 1–10.

Moreira, A., Prats-Iraola, P., Younis, M., Krieger, G., Hajnsek, I., & Papathanassiou, K. P. (2013). A tutorial on synthetic aperture radar. *IEEE Geoscience and Remote Sensing Magazine*, *1*(1), 6–43.

Oreiro, F. A., Fiore, M., D'Onofrio, E., Grismeyer, W., & Saraceno, M. (2013). Comparison of Global and Regional Tide Models Using Data from Satellite Altimeters and Tide Gauges in the Northeast Sector of the Antarctic Peninsula. *20 Years of Progress in Radar Altimatry*, *710*, 185.

Padman, L., Fricker, H. A., Coleman, R., Howard, S., & Erofeeva, L. (2002). A new tide model for the Antarctic ice shelves and seas. *Annals of Glaciology*, *34*, 247–254. https://doi.org/10.3189/172756402781817752

Padman, L., King, M., Goring, D., Corr, H., & Coleman, R. (2003). Ice-shelf elevation changes due to atmospheric pressure variations. *Journal of Glaciology*, *49*(167), 521–526. https://doi.org/10.3189/172756503781830386

Panchuk, K. (2019). 17.1 Types of Glaciers. In *Physical Geology, First University of Saskatchewan Edition*. https://openpress.usask.ca/physicalgeology/chapter/17-1-types-of-glaciers/

Richards, M. A., Scheer, J., Holm, W. A., & Melvin, W. L. (Eds.). (2010). *Principles of modern radar*. SciTech Pub.

Riedel, B., Nixdorf, U., Heinert, M., Eckstaller, A., & Mayer, C. (1999). The response of the Ekströmisen (Antarctica) grounding zone to tidal forcing. *Annals of Glaciology*, *29*, 239–242. https://doi.org/10.3189/172756499781821247

Rignot, E. (1996). Tidal motion, ice velocity and melt rate of Petermann Gletscher, Greenland, measured from radar interferometry. *Journal of Glaciology*, *42*(142), 476–485. https://doi.org/10.3189/S0022143000003464

Rignot, E. (1998). Hinge-line migration of Petermann Gletscher, north Greenland, detected using satellite-radar interferometry. *Journal of Glaciology*, *44*(148), 469–476. https://doi.org/10.3189/S0022143000001994

Rignot, E., Mouginot, J., Morlighem, M., Seroussi, H., & Scheuchl, B. (2014). Widespread, rapid grounding line retreat of Pine Island, Thwaites, Smith, and Kohler glaciers, West Antarctica, from 1992 to 2011. *Geophysical Research Letters*, *41*(10), 3502–3509. https://doi.org/10.1002/2014GL060140

Rignot, E., Mouginot, J., & Scheuchl, B. (2011). Antarctic grounding line mapping from differential satellite radar interferometry. *Geophysical Research Letters*, *38*(10). https://doi.org/10.1029/2011GL047109

Rosen, P. A., Hensley, S., Joughin, I. R., Li, F. K., Madsen, S. N., Rodriguez, E., & Goldstein, R. M. (2000). Synthetic aperture radar interferometry. *Proceedings of the IEEE*, *88*(3), 333–382. https://doi.org/10.1109/5.838084

Ross, D. A. (1995). *Introduction to Oceanography*. HarperCollinsCollegePublishers.

Roth, G., Matsuoka, K., Skoglund, A., Melvær, Y., & Tronstad, S. (2017). Quantarctica: A unique, open, standalone GIS package for Antarctic research and education. *EGU General Assembly Conference Abstracts*, 1973.

Rott, H. (2009). Advances in interferometric synthetic aperture radar (InSAR) in earth system science. *Progress in Physical Geography: Earth and Environment*, *33*(6), 769–791. https://doi.org/10.1177/0309133309350263

Scambos, T. A., Haran, T. M., Fahnestock, M. A., Painter, T. H., & Bohlander, J. (2007). MODIS-based Mosaic of Antarctica (MOA) data sets: Continent-wide surface morphology and snow grain size. *Remote Sensing of Environment*, *111*(2), 242–257. https://doi.org/10.1016/j.rse.2006.12.020

Shepherd, A., Ivins, E., Rignot, E., Smith, B., van den Broeke, M., Velicogna, I., Whitehouse, P., Briggs, K., Joughin, I., Krinner, G., Nowicki, S., Payne, T., Scambos, T., Schlegel, N., Geruo, A., Agosta, C., Ahlstrom, A., Bobonis, G., Barletta, v, … Wouters, B. (2018). Mass balance of the Antarctic Ice Sheet from 1992 to 2017. *Nature*, *558*, 219–222. https://doi.org/10.1038/s41586-018-0179-y

Sumich, J. L., & Morrissey, J. F. (2004). *Introduction to the Biology of Marine Life*. Jones & Bartlett Learning.

Thorvaldsen, A. (2017). Product User Guide (PUG) for the Antarctic_Ice_Sheet_cci Project of ESA's Climate Change Initiative, 2018. *Version*, *1.2*, 19.

Thurman, H. V. (1997). *Introductory Oceanography/With Geosciences on the Internet*. Prentice Hall.

Torres, R., Snoeij, P., Geudtner, D., Bibby, D., Davidson, M., Attema, E., Potin, P., Rommen, B., Floury, N., & Brown, M. (2012). GMES Sentinel-1 mission. *Remote Sensing of Environment*, *120*, 9–24.

US Department of Commerce, N. O. and A. A. (n.d.). *Tides and Water Levels, NOS Education Offering*. Retrieved March 3, 2021, from https://oceanservice.noaa.gov/education/tutorial_tides/welcome.html

Wild, C. T., Marsh, O. J., & Rack, W. (2018). Unraveling InSAR Observed Antarctic Ice-Shelf Flexure Using 2-D Elastic and Viscoelastic Modeling. *Frontiers in Earth Science*, *6*. https://doi.org/10.3389/feart.2018.00028